Geochemistry, Geophysics, Geosystems®

AGU ADVANCING EARTH AND SPACE SCIENCES

RESEARCH ARTICLE
10.1029/2023GC010982

Key Points:

- New 1-D velocity model relocates 1716 earthquakes with local magnitude ranging from 1 to 4.5 and *b*-value of 1.22 ± 0.06 in Turkana Depression
- Brittle strain localizes in narrow areas overlying uppermost mantle low velocity zones and avoids previously thinned crust of Mesozoic rift
- We redefine the modern Nubia-Somalia plate boundary across the Turkana Depression; only a part of the 300-km-wide region is active

Supporting Information:

Supporting Information may be found in the online version of this article.

Correspondence to:

M. Musila,
mmusila@tulane.edu

Citation:

Musila, M., Ebinger, C. J., Bastow, I. D., Sullivan, G., Oliva, S. J., Knappe, E., et al. (2023). Active deformation constraints on the Nubia-Somalia plate boundary through heterogenous lithosphere of the Turkana Depression. *Geochemistry, Geophysics, Geosystems*, *24*, e2023GC010982. https://doi.org/10.1029/2023GC010982

Received 3 APR 2023
Accepted 4 AUG 2023

Author Contributions:

Conceptualization: M. Musila, C. J. Ebinger, I. D. Bastow, R. Kounoudis, C. S. Ogden, R. Bendick
Formal analysis: M. Musila, G. Sullivan, S. J. Oliva, E. Knappe, M. Perry, R. Bendick, E. Kraus, F. Illsley-Kemp
Funding acquisition: C. J. Ebinger, I. D. Bastow, R. Bendick

Active Deformation Constraints on the Nubia-Somalia Plate Boundary Through Heterogenous Lithosphere of the Turkana Depression

M. Musila[1], C. J. Ebinger[1], I. D. Bastow[2], G. Sullivan[1], S. J. Oliva[3], E. Knappe[4], M. Perry[5], R. Kounoudis[2], C. S. Ogden[6], R. Bendick[7], S. Mwangi[8], N. Mariita[9], G. Kianji[8], E. Kraus[1], and F. Illsley-Kemp[10]

[1]Department of Earth and Environmental Sciences, Tulane University, New Orleans, LA, USA, [2]Department of Earth Science and Engineering, Imperial College, London, UK, [3]School of Earth and Ocean Sciences, University of Victoria, Victoria, BC, Canada, [4]Scripps Institution of Oceanography, San Diego, CA, USA, [5]Earth Observatory of Singapore, Nanyang Technical University, Singapore, Singapore, [6]School of Geography, Geology and the Environment, University of Leicester, Leicester, UK, [7]Department of Geosciences, University of Montana, Missoula, MT, USA, [8]Department of Earth and Climate Sciences, University of Nairobi, Nairobi, Kenya, [9]Geothermal Energy Training and Research Institute, Dedan Kimathi University of Technology, Nyeri, Kenya, [10]School of Geography, Environment and Earth Sciences, Victoria University of Wellington, Wellington, New Zealand

Abstract The role of lithospheric heterogeneities, presence or absence of melt, local and regional stresses, and gravitational potential energy in strain localization in continental rifts remains debated. We use new seismic and geodetic data to identify the location and orientation of the modern Nubia-Somalia plate boundary in the 300-km-wide zone between the southern Main Ethiopian Rift (MER) and Eastern Rift (ER) across the Mesozoic Anza rift in the Turkana Depression. This region exhibits lithospheric heterogeneity, 45 Ma-Recent magmatism, and more than 1,500 m of base-level elevation change, enabling the assessment of strain localization mechanisms. We relocate 1716 earthquakes using a new 1-D velocity model. Using a new local magnitude scaling with station corrections, we find $1 \leq M_L \leq 4.5$, and a *b*-value of 1.22 ± 0.06. We present 59 first motion and 3 full moment tensor inversions, and invert for opening directions. We use complementary geodetic displacement vectors and strain rates to describe the geodetic strain field. Our seismic and geodetic strain zones demonstrate that only a small part of the 300 km-wide region is currently active; low elevation and high-elevation regions are active, as are areas with and without Holocene magmatism. Variations in the active plate boundary's location, orientation and strain rate appear to correspond to lithospheric heterogeneities. In the MER-ER linkage zone, a belt of seismically fast mantle lithosphere generally lacking Recent magmatism is coincident with diffuse crustal deformation, whereas seismically slow mantle lithosphere and Recent magmatism are characterized by localized crustal strain; lithospheric heterogeneity drives strain localization.

Plain Language Summary Continental rifting involves the stretching, thinning, and heating of plates. Where present, magma adds heat, fluid, and new rock material into the plate, altering its physical and chemical properties. Pre-existing lithospheric thickness variations and crustal shear zones may also influence when and where rifting occurs. Rifting processes can be monitored by tracking the vertical and horizontal movement of plates, and by analyzing earthquake patterns. To address debates concerning the role of plate thinning, magmatism, and pre-rift lithospheric structures, we analyze new seismic and geodetic data from the Turkana Depression, a 300-km-wide region linking the Main Ethiopian Rift to the north and the Eastern Rift to the south. Additionally, the region has a failed Mesozoic rift with pre-existing crustal shear zones. We identify regions that are actively deforming, defining the active plate boundary. The breadth of the actively rifting zone decreases above mantle low-velocity zones, thinned mantle lithosphere, and/or hotter melt-infiltrated zones. We also find little to no evidence of reactivation of faults within the thin crust of a failed Mesozoic rift that is circumnavigated by the active rifting in the region. Our findings suggest that differences in the plate-scale physical and chemical properties dictate where and how faulting and magmatism occur.

1. Introduction

Data and models of the Cenozoic East African rift system and the Ethiopia-Yemen flood basalt province have offered invaluable insights into rifting processes above mantle plumes, yet questions remain regarding the

Investigation: M. Musila, C. J. Ebinger, I. D. Bastow, G. Sullivan, E. Knappe, M. Perry, R. Kounoudis, C. S. Ogden, R. Bendick, S. Mwangi, N. Mariita, G. Kianji
Methodology: M. Musila, C. J. Ebinger, G. Sullivan, S. J. Oliva, E. Knappe, M. Perry, R. Bendick, F. Illsley-Kemp
Project Administration: C. J. Ebinger, I. D. Bastow, R. Bendick, N. Mariita, G. Kianji
Resources: C. J. Ebinger, I. D. Bastow, R. Bendick
Supervision: C. J. Ebinger, I. D. Bastow, R. Bendick, N. Mariita
Visualization: M. Musila, C. J. Ebinger, I. D. Bastow, G. Sullivan, R. Kounoudis, C. S. Ogden, R. Bendick, S. Mwangi
Writing – original draft: M. Musila, E. Kraus
Writing – review & editing: M. Musila, C. J. Ebinger, I. D. Bastow, G. Sullivan, S. J. Oliva, E. Knappe, M. Perry, R. Kounoudis, C. S. Ogden, S. Mwangi, N. Mariita, F. Illsley-Kemp

processes controlling the localization of strain in old and thick continental lithosphere. Gravitational potential energy (GPE) (e.g., Gosh et al., 2009; Koptev & Ershov, 2010; Stamps et al., 2010), the presence or absence of magma and mantle dynamics (e.g., Buck, 2004; Furman et al., 2016), reactivation of pre-existing shear zones (e.g., Chorowicz, 2005), and lithospheric heterogeneities (e.g., Koptev et al., 2018; Kounoudis et al., 2021; Naliboff et al., 2012) are all considered factors that control strain localization in continental rifts, but their importance remains debated. New and existing seismic and geodetic data from the Turkana Depression region of East Africa offer new opportunities to evaluate the relative importance of these processes on rift localization and hence define the modern-day Nubia-Somalia plate boundary in the region.

The NW-trending Turkana Depression, a failed Mesozoic rift system, separates the uplifted Ethiopia-Yemen and East Africa plateaus that formed above one or more mantle plumes (e.g., Boyce et al., 2023; Chang & Van der Lee, 2011; George et al., 1998; Pik et al., 2006) (Figure 1a). The Oligocene-Recent East African rift zones transecting the plateaus overlap and link within the 300 km-wide Depression, but little was known of the age of structures, the kinematics of rift linkage, and the role of pre-existing structures in strain evolution (e.g., Knappe et al., 2020). This led to a range of proposed models for linkage of the Main Ethiopian, Eastern rifts (e.g., Brune et al., 2017; Corti et al., 2019; Ebinger et al., 2000; Morley et al., 1992), as well as possible linkage with the Western rift (e.g., Katumwehe et al., 2016).

The west to east migration of magmatism and sedimentary basins across the Turkana Depression since 30 Ma (Bruhn et al., 2011; Ebinger et al., 2000; Morley et al., 1992) suggests time variations in strain, and consequently changes in rift linkage along a changing plate boundary, but large data gaps prevented a clear picture of the breadth of the modern Nubia-Somalia boundary. New mantle imaging reveals heterogeneity at lithospheric scales associated with terranes accreted during the Pan African Orogeny (Kounoudis et al., 2021) (Figure 2). Recent crust and mantle lithosphere imaging (Kounoudis et al., 2021, 2023; Ogden et al., 2023) provide a strong context for our crustal strain studies. A recent geodetic study in the region has suggested that the high strain rates are localized in Lake Turkana rift basin (Figure 1b), the region with the lowest GPE (e.g., Knappe et al., 2020), but little was known of the broadly rifted area to the north of Lake Turkana.

Critical to assessing the hypotheses for strain localization and rift linkage in heterogeneous continental lithosphere is an understanding of the location and orientation of the modern-day Nubia-Somalia plate boundary, its relation to mantle velocity anomalies interpreted as compositional, thermal, and melt variations (Kounoudis et al., 2021, 2023), and the crustal thin zones in the Depression created by the superposition of two rifting episodes (Ogden et al., 2023). The Turkana Rift Array to Investigate Lithospheric Structure (TRAILS) seismic and geodetic studies infill a crucial data gap that enables us to define the active plate boundary, its kinematics, as well as the depth extent and geometry of fault zones. Using a new 1-D velocity model, we develop the first local seismicity catalog for the region from seismic data collected by the 34 broadband TRAILS stations (Figure 3; Figure S1 in Supporting Information S1). We present 59 first motion and 3 full moment tensor inversions to explore the kinematics of linkage between the <20 Ma Main Ethiopian Rift (MER) and the <27 Ma Eastern rift. Additionally, we analyze geodetic data from 20 campaign and continuous Global Navigation Satellite System (GNSS) stations from the TRAILS array (Figure 3; Figure S2 in Supporting Information S1; Knappe et al., 2020) providing complementary constraints on the regional geodetic strain field. We compare seismic and geodetic strain patterns with pre-existing Mesozoic rift structures (Figure 1b) and Pan-African accreted terranes to the Tanzania craton (Figure 2), crustal thickness variations (Ogden et al., 2023), and mantle imaging (Kounoudis et al., 2021, 2023) to evaluate their relative importance in the modern-day deformation. In doing so, we can evaluate and revise models of linkage between the MER and the ER systems, produce a revised modern-day plate boundary in the region and inform hazards in northern Kenya and southwestern Ethiopia.

2. Geodynamic and Tectonic Background

The ~300 km-wide zone of linkage between the MER and the ER spans the southern Ethiopian plateau, and the northern part of the East African plateau through the Turkana Depression (Figure 1b). The zone of linkage encompasses four sub-parallel rift basins: from southwest to northeast and from north to south in each strand: the Turkwel-Lokichar rift, Usno-Omo-Turkana rift, Aluma-Weyto-Chew Bahir-Kino Sogo rift and the Chamo-Segen-Ririba rift, which is the southernmost continuation of the MER (Figure 1b). The Turkana rift connects to the 60–80 km wide Eastern rift (ER) through the Suguta rift south of Lake Turkana (Figure 1b).

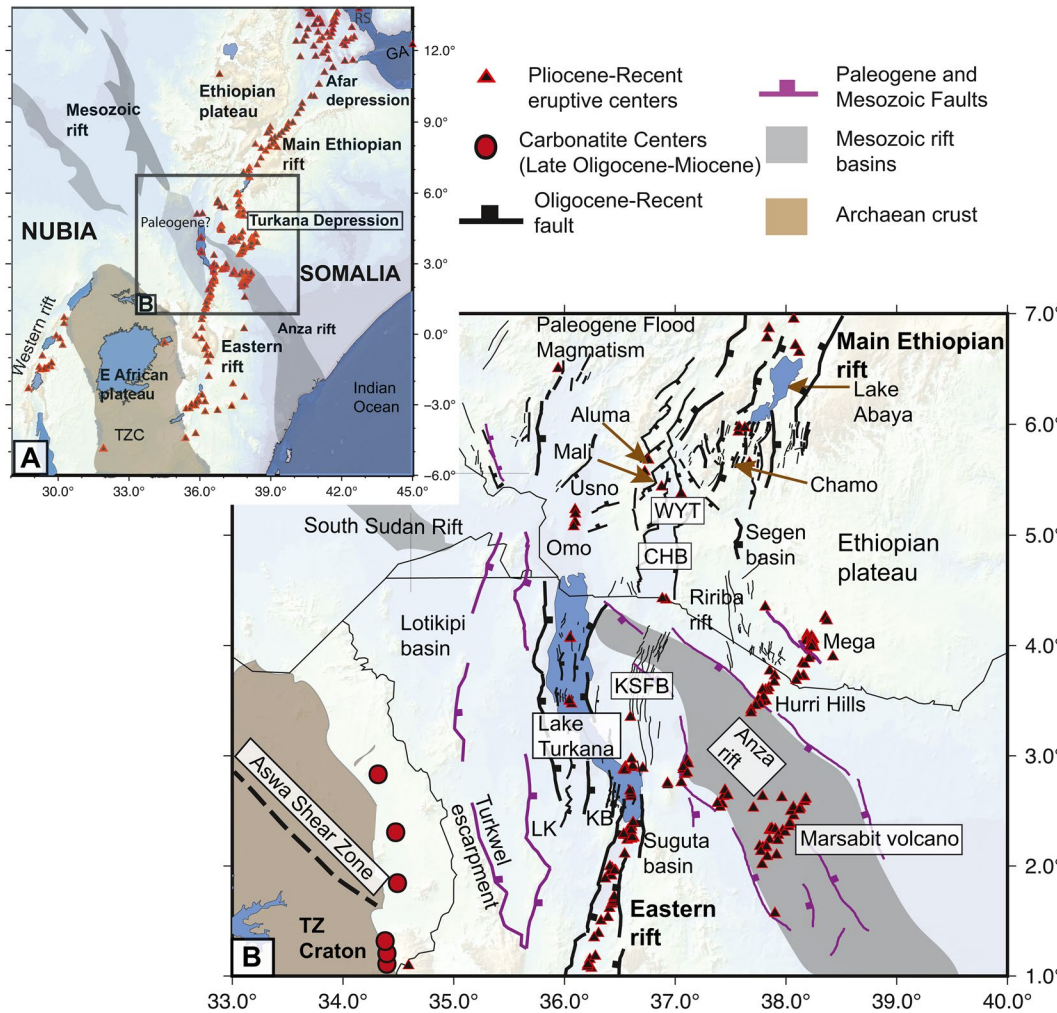

Figure 1. (a) Turkana Depression relative to the Main Ethiopian Rift (MER), Eastern rift (ER) and Western rift in East Africa. Mesozoic-Paleogene rift basins are shaded in gray (after Ebinger et al., 2000; Purcell, 2018; Boone, 2018) and Pliocene-Recent eruptive centers are in black triangles with a red outline (after Global Volcanism Program, 2013; Sullivan, 2023). TZC is the Archean Tanzania craton. RS and GA are the Red Sea and Gulf of Aden, respectively. (b) Zone of linkage between the MER and ER showing the Turkana Depression with Mesozoic-Paleogene and Oligocene-Recent faults and basins in purple and black, respectively (after Corti et al., 2019; Davidson, 1983; Ebinger et al., 2000; Schofield et al., 2021; Franceschini et al., 2020; Morley, 2020). Four sub-parallel rift strands from southwest to northeast: Turkwel-Lokichar (LK) rift, Suguta-Lake Turkana-Omo-Usno rift, Kino Sogo (KSFB)-Chew Bahir (CHB)-Weyto (WYT) rift and Ririba-Segen-Chamo rift. Kerio basin (KB). Pliocene-Recent eruptive centers are in black triangles with a red outline. TZ craton is the Tanzania craton (outline after Westerhof et al., 2014) with 20–25 Ma carbonatite volcanoes denoted by red circles (after Cote et al., 2018; Muirhead et al., 2020). The Mesozoic Anza rift basin in gray shading (after Boone, 2018; Purcell, 2018). The dashed line is the Neoproterozoic Aswa shear zone (after Katumwehe et al., 2016).

Pre-existing lithospheric terranes of northeastern Africa include the >150 km-thick lithosphere of the Archean Tanzania craton and the ~120 km-thick Pan-African orogenic belt (e.g., Boyce et al., 2023; Emry et al., 2019). The Pan-African orogeny (700–550 Ma) led to the accretion of island-arcs and micro-continents to the Tanzania craton (e.g., Fritz et al., 2013; Stern et al., 2012; Teklay et al., 1998). A NW-striking high-grade ultramafic arc complex occurs within the Pan-African lithosphere of southwestern Ethiopia (e.g., Davidson & Rex, 1980) (Figure 2). West of the Turkana Depression at the northeastern side of the Tanzanian craton is the NW-striking Neoproterozoic Aswa shear zone (660–690 Ma) that sutured two cratons (e.g., Katumwehe et al., 2016).

Three main rifting phases occurred in the Turkana Depression: the Cretaceous (130–80 Ma), Paleogene (65–50 Ma) and Miocene to Recent (25–0 Ma) (Ebinger et al., 2000; Morley et al., 1992; Torres Acosta et al., 2015). The largely amagmatic NW-SE failed Mesozoic rift spans the Central African rift through the Turkana Depression

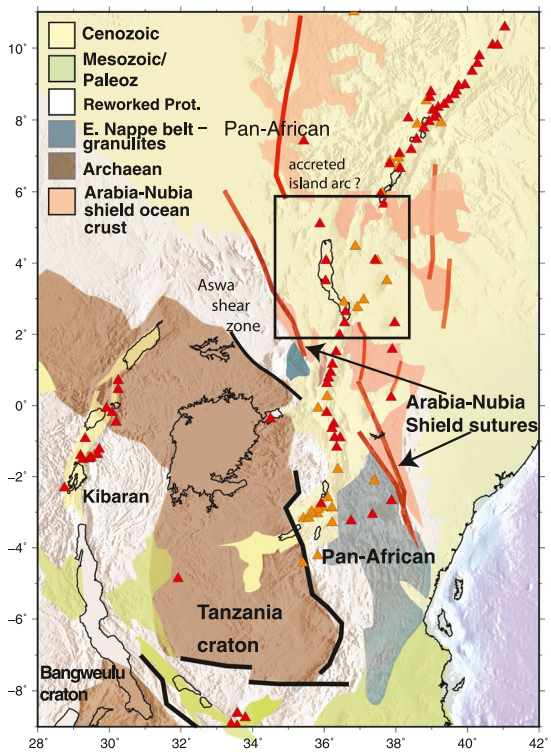

Figure 2. Tectonic units spanning Archean cratons, Pan African Orogeny and Proterozoic-Paleozoic accreted terranes. Overlain are Pan-African suture zones (red lines) that occurred in distinct phases: the ~850–620 Ma Arabian-Nubian shield with predominant juvenile Neoproterozoic crust and the ~650–620 Eastern Nappe complex with granulite-facies metamorphism (after Fritz et al., 2013). Pleistocene volcanoes (orange) and Holocene volcanoes (red) denoted by triangles (Global Volcanism Program, 2013). The study area is delineated by the black box.

to the Anza graben (e.g., Morley et al., 1999). Some parts of the Mesozoic rift show evidence of renewed faulting and exhumation at 60–45 Ma (e.g., Morley et al., 1999; Torres Acosta et al., 2015). These Cretaceous-Paleogene sedimentary basins host 2–10 km thick sedimentary strata with minor volcanic units, as determined from the modeling of gravity and magnetic data and oil wildcat wells (e.g., Dindi, 1994; Morley et al., 1999). Between the poorly understood Paleogene rifting event and the onset of extension in East Africa, one or more plumes impinged on the base of the lithosphere, resulting in flood magmatism (e.g., George et al., 1998; Pik et al., 2006) in the southwestern part of the Ethiopian plateau, and what is now the southern MER (Figure 1b). This ~45 to 35 Ma period of magmatism is not associated with any surface extension, although dikes feeding the lavas must have caused some crustal extension (e.g., Steiner et al., 2022). The southern extent of the flood basalts is ~5.5°N (Steiner et al., 2022).

Between 25 and 27 Ma, there was a pulse of basaltic volcanism and the initiation of faulting west of Lake Turkana, leading to the formation of half-graben basins (Morley et al., 1999; Wescott et al., 1999). From 18 to 25 Ma, the eastern margin of the Tanzania craton experienced carbonatite volcanism (e.g., Cote et al., 2018; Muirhead et al., 2020). Time-space patterns of magmatism, faulting, and basin subsidence determined from surface outcrops, scientific drilling, and exploration well data indicate a west to east migration of rifting and magmatism in northern Kenya (Morley et al., 1999; Schofield et al., 2021), whereas geochronology is too sparse to determine in southwestern Ethiopia (e.g., Ebinger et al., 2000; Philippon et al., 2014).

Seismic reflection data calibrated by well data indicate that the Turkwel-Lokichar rift contains 5–7 km of Miocene-Recent sedimentary and volcanic strata (Schofield et al., 2021). Beneath Lake Turkana, 2–5 km of sedimentary strata cut by sub-N-S striking intrabasinal faults with localized magmatic intrusions have been imaged, although Mesozoic strata may underlie some parts of the Turkana rift (Dunkleman et al., 1989; Muirhead et al., 2022). The eastward migration of faulting and magmatism continues through to Holocene time: east of Lake Turkana, there are unfaulted ~3 Ma-recent basaltic shield complexes and fissures (e.g., Guth, 2016) (Figure 1b). The 25 Ma-Recent eastward migration of magmatism and faulting produced the unusual breadth of the Turkana Depression (e.g., Ebinger et al., 2000; Knappe et al., 2020; Morley et al., 1992).

Global tomographic models support the hypothesis that the African superplume rises from the core mantle boundary beneath southern Africa to the base of the lithosphere beneath East Africa (e.g., French & Romanowicz, 2015; Ritsema et al., 2011). Regional body and surface wave models image details within the super plume province and reveal two or more whole-mantle slow wave speed anomalies (Boyce et al., 2023; Chang et al., 2020; Emry et al., 2019). These separately imaged plumes are suggested to have influenced the spatial and temporal variations in mantle sources for magma in the EAR (e.g., Boyce et al., 2023; Chang et al., 2020). Using the TRAILS database, Kounoudis et al. (2021) imaged velocity variations in the mantle at depth ranges of ~75–600 km. They showed a continuity of the slow wave speed anomaly from the Ethiopian plateau underneath the Turkana Depression to the East African plateau. The seismically slow wavespeed anomaly is interpreted as a zone of mantle lithosphere thinning, heating, and/or melt infiltration (Kounoudis et al., 2021, 2023). A second prominent feature is a NW-trending high velocity zone at depths <150 km that coincides with a belt of mafic/ultramafic rocks interpreted as a refractory Proterozoic lithosphere (Kounoudis et al., 2021). Kounoudis et al. (2021) proposed that the higher velocity terrane may have served as a stronger zone that influenced Mesozoic and Cenozoic strain localization in the Turkana Depression. Surface wave tomographic models indicate the continuation of the refractory accreted terrane at the uppermost parts of the mantle lithosphere at depths of 50–70 km (Kounoudis et al., 2023). The same study showed that mantle beneath the NW-trending Mesozoic Anza rift is relatively refractory, with shear wavespeeds of >4.5 km/s.

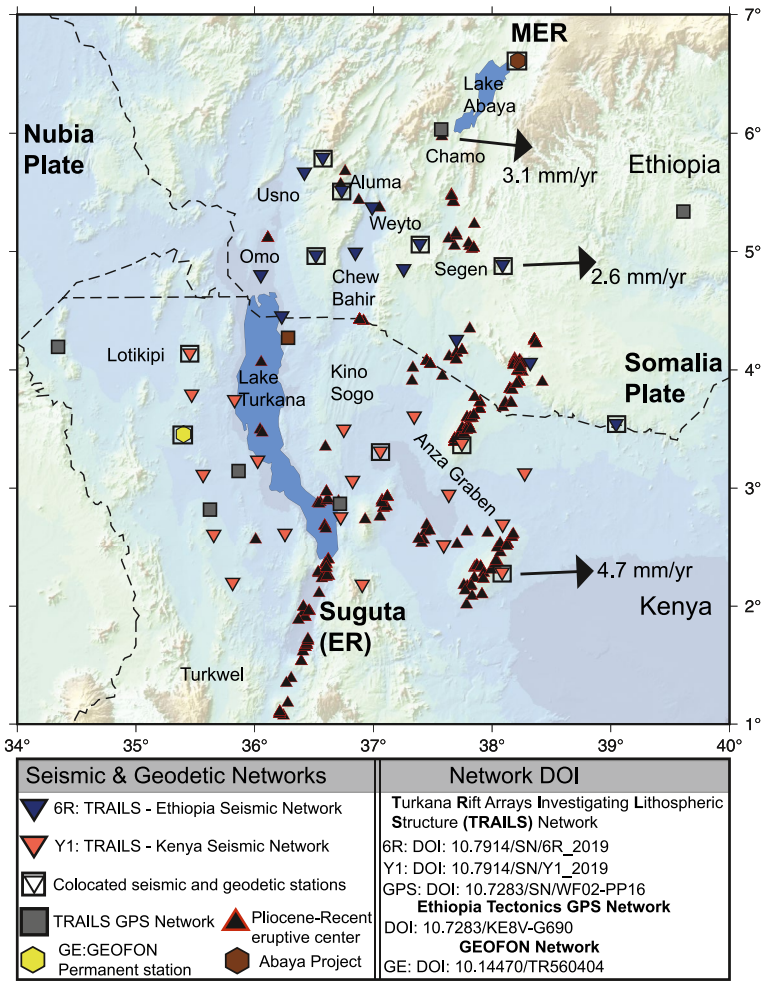

Figure 3. Inverted triangles are the Turkana Rift Array to Investigate Lithospheric Structure (TRAILS) project seismic stations (Ebinger (2018) Y1 network = orange; Bastow (2019) 6R network = blue. Other seismic networks (GEOFON Data Center (1993) = yellow hexagon; Ogden et al. (2021) network = brown hexagon). Gray square boxes show the spatial distribution of 12 continuous and eight campaign Global Navigation Satellite System (GNSS) stations. GNNS and seismic stations that are collocated have seismic stations overlain with a black box. Black arrows indicate plate motion in mm/yr relative to the fixed Nubia plate (after Kogan et al., 2012; Knappe et al., 2020). Note that 2.6 mm/yr velocity in southern MER is an underestimation of velocity due to the lack of GNSS stations in South Sudan (Figure S2 in Supporting Information S1). Pliocene-Recent eruptive centers are black triangles with red outline (after Global Volcanism Program, 2013; Sullivan, 2023).

Several studies have probed the crustal structure of parts of the Turkana Depression. A crustal-scale refraction/wide-angle reflection seismic profile along the length of Lake Turkana determined a crustal thickness of 20 km (Mechie et al., 1994; Prodehl et al., 1994). Rayleigh wave dispersion studies using permanent and temporary broadband seismic stations outside the Turkana Depression reported crustal thickness of 25 ± 5 km (Benoit et al., 2006). Based on new receiver function analyses and surface wave studies using data from the TRAILS network and nearby surrounding seismic stations, Moho depths within the Depression are 21–30 km relative to the 34–38 km in unrifted areas west and east of the TRAILS array, respectively (Ogden et al., 2023). The thinnest crust underlies the Lokichar, Omo-Turkana and Chew Bahir rifts, all of which lie within the area affected by Mesozoic rifting; crustal stretching factors are ≥1.9 (Ogden et al., 2023). The Turkana Depression, therefore, is a consequence of twice-stretched crust with as much as 500 m of dynamic support (Kounoudis et al., 2021; Ogden et al., 2023). Although the lithosphere had largely equilibrated before the onset of rifting at ~27 Ma, the crustal thinning is permanent. Hence, comparatively strong, dense mantle lithosphere occupies a larger percentage of the lithosphere beneath the Mesozoic rifts, potentially making these zones stronger than areas with thicker crust. Despite the 45 My history of magmatism in some parts of the study area, the bulk crust Vp/Vs in the study area

is <1.75, except in some localized regions east of Lake Turkana with bulk Vp/Vs of >1.8 that may signify the influence of magmatic modification (Ogden et al., 2023).

The Main Ethiopian Rift (MER) marks the boundary between the stable Nubia plate and the Somalia plate to the east, which are diverging at 5–7 mm yr^{-1} from data (Birhanu et al., 2016) and models (Stamps et al., 2021). Within the Turkana Depression and southward in the Eastern Rift (ER), the Victoria microplate lies between the Western and Eastern rift (Figure 1a). Campaign and continuous GNSS data record an average of ∼4.7 mm yr^{-1} of eastward extension relative to stable Nubia (Knappe et al., 2020) (Figure 3). GNSS strain patterns indicate that the present-day deformation is localized in the half-graben basins of Lake Turkana, the area with the lowest GPE (Knappe et al., 2020). Although Chorowicz (2005) and Katumwehe et al. (2016) kinematically link the Eastern and Western rifts via reactivation of the Proterozoic Aswa shear zone as a left lateral transform fault, the absence of earthquake activity and lack of motion from geodetic data argue against linkage to the Western rift through the Turkana Depression (Knappe et al., 2020).

Analog and numerical models of two propagating rift zones suggest that the existence of the stretched lithosphere beneath the Anza graben created an unusually broad zone of interaction between the southward-propagating MER and the northward-propagating ER (Brune et al., 2017), but geological data show that basins in the Depression formed diachronously, and along-axis propagation was away from the Turkana Depression. Corti et al. (2019) used remote sensing and field mapping to propose that the unusual rift width is caused by the southward propagation of the MER through the Ririba rift, and the subsequent abandonment of the connection in the past 1 Ma, but the kinematics of current linkage remained unclear.

3. Data

We analyze seismic data collected from the Turkana Rift Array to Investigate Lithospheric Structure (TRAILS) project and incorporate results from GNSS data acquisition and analyses, building on Knappe et al. (2020). The project comprises 34 broadband seismic stations located in northwestern Kenya (network Y1, Ebinger, 2018) and southwestern Ethiopia (network 6R, Bastow, 2019), 12 continuous and eight campaign Global Navigation Satellite System (GNSS) stations (Figure 3, Figures S1 and S2 in Supporting Information S1). The GNSS stations are spaced 200–300 km apart with the array aperture limited to the west near South Sudan due to security concerns (Figure 3; Figure S2 in Supporting Information S1). The TRAILS project stations were deployed from January 2019 to June 2021. In Kenya and Ethiopia, the earthquakes were detected by Güralp CMG3T and CMG-ESP sensors. The 6R and Y1 seismic networks have Reftek and Q330 data loggers, respectively. Stations in Kenya recorded at 100 sps; smaller data logger storage sizes in Ethiopia meant that only a few low noise stations recorded at 100 sps; the remainder recorded at 50 sps. Data from two additional GEOFON STS2 sensors in Kenya (LODK, KIBK) and a Güralp 6TD sensor and datalogger in southern Ethiopia (ARGA, Ogden et al., 2021) are also incorporated into the database (Figure 3; Figure S1 in Supporting Information S1).

We use a Butterworth bandpass filter between 1.5 and 10 Hz and manually pick P- and S- wave phases. The first arrivals of the P-wave were picked from the vertical channel whereas the S-wave picks were made on the transverse channel, after initial location. All earthquakes considered in this study are confined within the seismic network geometry (6R and Y1, Figure 3) to minimize the earthquakes' location uncertainties.

4. Methods

4.1. Velocity Model

The absolute earthquake locations of 1716 events are first located using a velocity model obtained from the Turkana area seismic refraction/wide-angle reflection KRISP profile along the length of the Lake Turkana basin (Mechie et al., 1994). We use the arrival times of a subset of 237 earthquakes distributed across the broadly rifted southern MER and Lake Turkana active rifts (Figure S1 in Supporting Information S1) and with 10 or more P-wave arrivals to find a new 1-D velocity model that minimizes the earthquakes' travel time residuals (Kissling et al., 1995). Since most of the local earthquakes in our catalog are relocated at upper-to-lower crustal depths (<25 km) (Ogden et al., 2023), we damped our 1-D velocity inversions at the average Moho (depths > 25 km). The new velocity model and the station corrections are then used to relocate the entire database and provide absolute earthquake locations.

4.2. Earthquake Locations and Relocations

The absolute locations of the earthquakes were determined using the HYPOINVERSE2000 algorithm (Klein, 2000) and the new 1-D velocity model (Figure 5; Figure S3 in Supporting Information S1). Relative locations of spatial clusters that occurred beneath the Usno-Omo-Turkana, Weyto-Chew Bahir, and Segen rifts are calculated using the hypoDD double-difference algorithm and the 1-D velocity model (Waldhauser & Ellsworth, 2000) (Figure 6). The double-difference algorithm relocates earthquake pairs based on these two conditions: earthquake pairs having separation distances that are less than their hypocentral depths, and earthquake pairs with ray paths that are less than the lateral scale of crustal heterogeneity (Waldhauser & Ellsworth, 2000). The relative relocations are done relative to the clusters' centroid.

Input data for the double-differencing algorithm are the lag times from the cross-correlated P-wave onsets. The cross-correlation was done on waveforms bandpass filtered at 1.5–10 Hz. The correlation process involves defining short window sizes ranging from 0.3 to 0.6 s around one of the earthquake pairs and using that window to take a sliding dot product to the other earthquake pair. The short time window selected enables the cross-correlation around the P-wave onset section of the waveform. Waveform similarity is then quantified by the cross-correlation coefficient. The event pairs with cross-correlation coefficient $\geq$0.6 are then used to stack the waveforms, resulting in improved P-wave arrival times for well-correlated pairs of earthquakes. In hypoDD, the lag times are used to adjust the vector difference between the earthquake pairs while updating their locations through successive iterations (Waldhauser & Ellsworth, 2000). Uncertainties in the relative earthquake locations are estimated using the Singular Value Decomposition (SVD) by using a subset of ~50 randomly selected events per spatial cluster.

4.3. Earthquake Magnitude and *b*-Value

Local magnitudes are estimated using measurements of the maximum amplitude of the shear wave arrivals as measured on a Wood-Anderson seismograph and a new magnitude scaling with station corrections, as described in Supporting Information S1. The *b*-value describes the magnitude frequency distribution of earthquakes, whereby a smaller *b*-value indicates a high proportion of large earthquakes (Kanamori, 1983). The *b*-value is inversely proportional to plate stress (e.g., Scholz, 2015). The frequency-magnitude analysis is used to determine the magnitude of completeness (M_c), the minimum magnitude of the earthquakes that are well determined in the catalog, assuming a Gutenberg-Richter law, as outlined in the Supporting Information S1.

4.4. Source Mechanisms

Source mechanism solutions are determined using the polarity of the first motion of the P-wave arrival times from visual inspection and using the take-off angle and azimuth to the station using output from HYPOINVERSE (Snoke, 1984). The FOCMEC program determines and displays the strike, dip, and rake of the primary and auxiliary nodal planes that fit the data using a grid search approach. The criteria used to select source mechanisms in this study include (a) earthquakes with more than 10 first P-wave arrivals with azimuthal gap $\leq$130°, (b) $2\sigma < |10°|$ deviation for the source mechanisms' strike dip and rake, (c) allowing one P-phase error if it is within 5° of a nodal plane to account for the sensitivity of take-off angles to depth and lateral crustal heterogeneity. Given that take-off angles are sensitive to depth, we use waveform modeling of the largest magnitude earthquakes in the data set ($M_L \geq 3.8$) to evaluate the earthquakes' focal mechanisms with depth as a free parameter. In our Full Moment Tensor inversions (FMT), we fit a synthetic waveform to the surface waves (Rayleigh and Love wave) parts of the local earthquakes bandpass filtered to a range within 0.02–0.10 Hz following Oliva et al. (2019) and as outlined in the Supporting Information S1. Surface waves are less sensitive to small scale crustal heterogeneity, providing an independent method of determining the earthquake's depth and type of source mechanism.

4.5. Stress Inversion and Kostrov Summation

We recognize that the earthquake cycle in the rift zones is much longer than the ~2.5 years of seismic data recorded by the TRAILS project. While we also used the teleseismically detected earthquakes spanning 1983–2021 in our analyses (e.g., Ekström et al., 2012), we still acknowledge that the ~40-year duration of the CMT catalog may also be shorter than the earthquake cycle in our study area. Using these two available seismic records, we independently estimate and compare the plate velocities and strain rates. We use two approaches

to quantify the crustal principal stress regime: inversion for principal stresses using the grid search algorithm MSATSI (Martinez-Garzon et al., 2014) and Kostrov summation that provides the average individual moment tensor components weighted by their magnitudes (Kostrov, 1974).

The MSATSI algorithm estimates the stress-field orientation from the nodal planes of the earthquake focal mechanisms (Martinez-Garzon et al., 2014). The MSATSI algorithm uses a grid search to estimate the deviatoric stress tensor and the orientations of the principal stresses. Uncertainties are quantified using the bootstrap method with 200 solutions and using 95% confidence limits. In each iteration, one nodal plane is used with the preferred nodal plane being the one oriented to the given state of stress (Vavryčuk, 2014).

Kostrov summation simulates the deformation of a finite-width plate boundary and sums the individual moment tensor components, weighted by their magnitudes (Kostrov, 1974). For teleseismically detected earthquakes, we used depth-calibrated source mechanism results from waveform modeling (Craig & Jackson, 2021; Foster & Jackson, 1998) to address the 20–30 km horizontal uncertainties and depth uncertainties associated with Global CMT solutions with fixed depths (e.g., Ekström et al., 2012). Additionally, we incorporated waveform modeling source parameter results for the Mw 5, 3 May 2020, teleseismically detected earthquake recorded by the local TRAILS array to provide depth calibration of the event. The source mechanism solutions of the earthquakes recorded at teleseismic distances in the region are then used to invert strain rates and principal stress orientations and compare the stress orientations to those inverted from local earthquakes and geodetic displacement vectors, as outlined in the Supporting Information S1.

4.6. GNSS Velocity and Strain Rates

To accurately constrain the surface kinematics, observations from our GNSS network are combined with data collected from 2012 to 2021 from stations located within Ethiopia and Kenya and International GNSS Continuous stations in Africa, Europe, and Asia to define a stable reference frame. The TRAILS project consisted of the installation of 9 new continuous sites in January and February of 2019 and serviced 3 existing continuous stations (NEGE, XTBI, XTBT) and 5 campaign stations, the installation of one campaign station in January 2020 (XHRI), and the re-occupation of 3 campaign stations in 2020 (KEYA, SEOL, XHRI), and 2 in 2021 (XHRI and SEOL) (Figure 3 and Figure S2 in Supporting Information S1). These data were combined with raw data from 38 regional sites, including several International GNSS Service reference stations. We process the data using the GAMIT/GLOBK software package (Herring et al., 2010) following the procedure described in Reilinger et al. (2006). We calculate daily position time series using GAMIT. These time series are then inspected for any outliers and transient signals, which are then removed. The time series are then binned and averaged into fortnightly position estimates. We then use GLOBK's Kalman filter to estimate linear velocities within the International Terrestrial Reference Frame 2014 (ITRF14) (Altamimi et al., 2016), incorporating a random walk noise model to account for systematic errors in the continuous sites. For the campaign stations that do not have enough data to calculate a site-specific noise model, we apply a median noise model derived from all the continuous stations. The resulting linear velocities, representative of long-term tectonic deformation rates, are then rotated into a stable Nubia reference frame using the ITRF14-Nubia angular velocity calculated by Altamimi et al. (2017).

Once site velocities are determined, the sites are separated into 3 rift normal transects and a sigmoid is fitted to the east velocity (primary direction of extension, e.g., Saria et al., 2013; Knappe et al., 2020) as a function of distance along the profile following Kogan et al. (2012) and utilizing the station uncertainties as weights. The sigmoid function is defined as follows:

$$v_x = v_{\min} + \frac{v_{\max}}{1 + \exp\left(\frac{x_{d^2v/dx^2} - x}{\rho}\right)}$$

where v_x is the velocity, $v_{\min}$ and $v_{\max}$ are the minimum and maximum extension velocities, respectively, x_{d^2v/dx^2} is the inflection point along the profile that defines the location of maximum extension, and ρ is the sigmoid rate coefficient.

We calculate the first-order geodetic strain rates by first averaging all the annual velocities of GNSS stations located in the deforming zones of interest. We divide the annual average velocities of the GNSS stations in the deforming zones of interest with their associated zone lengths (L1), the length parallel to the extension direction

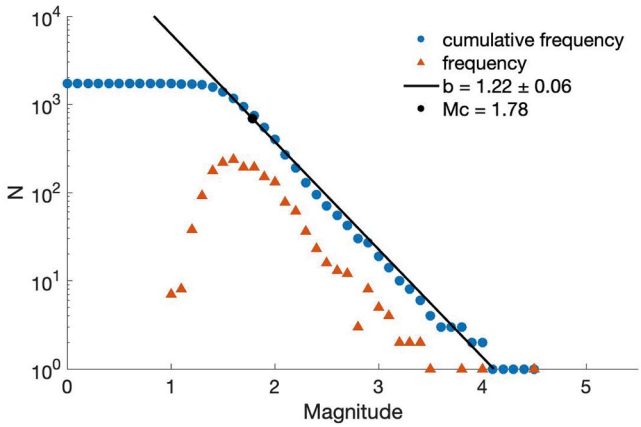

Figure 4. The *b*-value determination using the maximum likelihood method estimate in the Turkana Depression is 1.22 ± 0.06. The magnitude of completeness (M_C) is 1.78 after accounting for the correction factor +0.2 from the maximum curvature method (Woessner & Wiemer, 2005).

in our study area (Figure 3), to constrain the geodetic strain rates consistent with our Kostrov Summation calculations. To confirm the validity of our geodetic strain rates, we additionally took the derivative of the GNSS velocity profiles in the zones of interest and obtained comparable strain rates (e.g., Knappe et al., 2020).

5. Results and Interpretations

5.1. 1-D Crustal Velocity Model

The new 1-D velocity model was stable at depths ≤25 km, which coincides with the Moho beneath some areas, and the lower crust elsewhere in the study area (Ogden et al., 2023). The regression of all the local earthquakes plotted in the S-P arrival times versus P- wave arrival times space gave a Vp/Vs ratio of ∼1.75 (Figure S4 in Supporting Information S1), which is comparable to the bulk crustal Vp/Vs of ≤1.75 from receiver function analysis (Ogden et al., 2023).

5.2. Magnitudes and *b*-Value

Based on our new local magnitude scaling (see Supporting Information S1), the 1716 local earthquakes recorded in ∼2.5 years in the Depression have a range of $1.0 \leq M_L \leq 4.5$ and the *b*-value is 1.22 ± 0.06 (Figures 4 and 5). The *b*-value estimates north and south of 5° N, delineating southwestern Ethiopia to northern Kenya, are comparable to the regional estimate of 1.39 ± 0.07 for the northern sector of the Eastern rift, including the southern Turkana Depression (Shah, 1986). Our values are comparable to the *b*-values of 1.13 ± 0.05 (Keir et al., 2006) in the central MER, but much larger than the estimate of 0.69 ± 0.08 for the Lake Abaya rift zone based on a 1-year study (Ogden et al., 2021).

With a crustal thickness of 21–30 km in the Turkana Depression (Ogden et al., 2023), we determined the *b*-value variations between the upper (≤10 km) and mid-to-lower (≥10 km) crust. In the upper crust, there are 1223 earthquakes with a *b*-value of 1.36 ± 0.11 (Figure S7 in Supporting Information S1), whereas at the mid-to-lower crustal depths, there are 493 earthquakes with a low *b*-value of 1.16 ± 0.09 (Figure S8 in Supporting Information S1). The lower *b*-value at mid-to-lower crustal depths may be biased owing to the small number of earthquakes (e.g., Muluneh et al., 2020). Other plausible explanations for *b*-value variations at depth include the linear decrease in *b*-values with decrease in differential stress (Scholz, 2015), changes in stress conditions and/or crustal heterogeneity and fluid diffusion (Marzocchi et al., 2020).

5.3. Earthquake Locations

5.3.1. Absolute Locations

Quality control of the 1716 earthquakes in our local earthquake catalog include earthquakes with azimuthal gaps <120° and depth uncertainties <8 km. The mean horizontal uncertainty was 3.2 km, and the mean depth uncertainty was 2.1 km. Our event location for the 3 May 2020, Mw 5 (M_L 4.5) provides a measure of uncertainties in the Global CMT catalog: our horizontal location is 11 km southeast of the Global CMT location. The GCMT depth of 13.9 km is within the limits of our depth uncertainty estimates (14.2 ± 1.5 km).

In southern Ethiopia, seismicity is largely localized to three ∼100 km-wide N-S to NNE-trending zones of basins and their flexurally uplifted flanks: the Usno-Omo-Turkana basins; Aluma-Weyto-Chew Bahir-Kino Sogo rift; Chamo-Segen-Ririba rift (Figure 5). We briefly summarize seismicity patterns to outline the logic of cluster analyses and stress inversion groupings and integrate results along three cross sections in the Discussion.

5.3.1.1. Chamo-Segen-Ririba Rift Zone (MER)

Shallow seismicity is concentrated along the western side of the Segen rift. Owing to the ARGA seismic station in the Abaya basin during the period from July 2019 to February 2020 (Ogden et al., 2021), the apparent gap in seismicity in the NNE-trending Chamo basin is probably representative (Box A, Figure 5). The Ririba rift is largely aseismic.

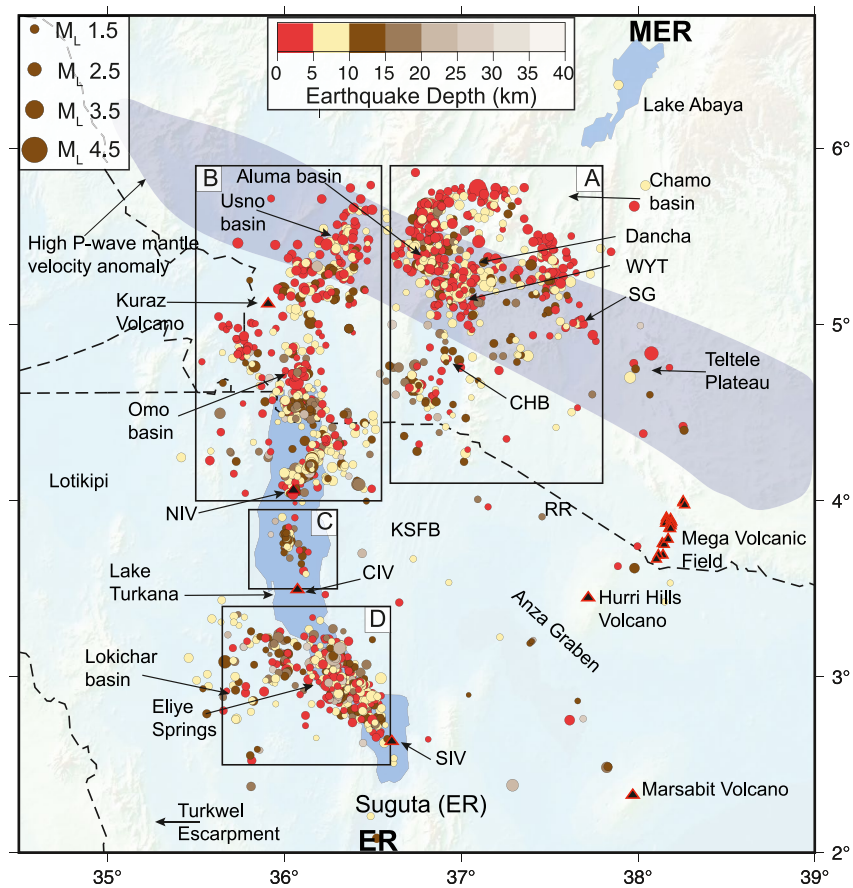

Figure 5. Absolute earthquake locations are color-coded by depth and scaled by magnitude. Boxes A, B, C, and D enclose clusters that were analyzed using the double-difference algorithm (Figure 6). The high P-wave mantle velocity anomaly in southern MER, imaged at depths of 50–100 km and denoted by the purple ribbon, is interpreted as a Pan African accreted terrain (Kounoudis et al., 2021). MER, WYT, CHB, SG, RR, KSFB, and ER are the Main Ethiopian Rift, Weyto, Chew Bahir, Segen graben, Ririba rift, Kino Sogo Fault Belt, Suguta, and Eastern rift, respectively. Pliocene-Recent eruptive centers include North, Central, and South Islands labeled as NIV, CIV and SIV, respectively. Recent volcanic fields in black triangles with red outlines.

5.3.1.2. Teltele Plateau

Earthquakes occur at the edge of the Teltele plateau, including an M_L 3 earthquake (~4.8°N, 38°E) (Figure 5). The Mega volcanic field is largely aseismic.

5.3.1.3. Aluma-Mali-Weyto-Chew Bahir

The Aluma basin experienced multiple clusters of earthquakes at depths 25 km to the surface during the study period, including M_L 4 and M_L 3.8 earthquakes. The number of earthquakes increases southward from the Aluma basin to the northern Weyto basin where the rift faults also strike NNE (Box A, Figure 5). The seismicity is most intense in the eastward jog in the rift trace between the Aluma and Weyto basins. Seismicity is less focused than along the Turkana rift, and there is no clear gap between this zone and the Chamo-Segen-Ririba rift zone to the east (Box A, Figure 5). By comparison, the Chew Bahir rift is less active and characterized by lower crustal earthquakes in this area of <25 km-thick crust (Ogden et al., 2023).

5.3.1.4. Usno-Omo-Turkana Basins

The NNE-trending Usno basin is characterized by an ~50 km-wide zone of primarily shallow (<10 km-deep) seismicity that broadens where the rift faults shift to a N-S orientation at the northern end of the Omo basin (Box B, Figure 5). Here, two distinct zones of seismicity spanning a depth of 15 km to surface are observed: a NNW-trending zone and a ~30 km-wide zone of seismicity that continues southward to North Island Volcano

Table 1
Number of Relocated Earthquakes, Maximum Horizontal Error, and Depth Uncertainties of the Relocated Earthquakes (Figure 6) in Each of the 4 Zones Shown by Boxes in Figure 5

Zone	N	Δhoriz (km)	Δz (km)
Box A	198	<0.9	<1.5
Box B	205	<0.04	<0.06
Box C	39	<0.03	<0.05
Box D	306	<0.8	<0.5

Note. Horiz is horizontal.

(NIV, Box B, Figure 5). An intense zone of primarily lower crustal seismicity lies along the eastern side of the northern Turkana basin (Box B, Figure 5), followed by a tight cluster spanning 20 km to the surface slightly north of Central Island Volcano (CIV, Box C, Figure 5). A largely aseismic zone separates seismicity at Central Island with the most intense concentration of seismicity in the southern Turkana rift, which coincides with the eastward jog in the rift, linking the Turkana rift with the narrow Suguta rift in the Eastern Rift (Box D, Figure 5). This area, the Eliye Springs kink, is the site of the 3 May 2020, Mw 5.0 (M_L 4.5) earthquake.

5.3.1.5. *Largely Aseismic Zones*

Basins west of the Omo-Turkana rift (e.g., Turkwel escarpment, Lotikipi, Lokichar) are largely aseismic, consistent with the eastward migration of the depocenter and magmatism between ~15 Ma and ~3 Ma (e.g., Ebinger et al., 2000; Morley et al., 1992; Schofield et al., 2021). Shallow earthquakes west of Lake Turkana may be quarry blasts. The exception is the Lokichar basin west of Lake Turkana, which experienced earthquakes in the lower crust (Box D, Figure 5). East of Lake Turkana, the Kino Sogo fault belt and the largely unfaulted shield volcanic complexes, for example, Marsabit and Hurri Hills, are also largely aseismic (Figure 5). The Anza graben is largely aseismic, as well. Given these spatial patterns, as well as background geology and geophysics, we relocate and interpret earthquakes in the 4 separate regions, as shown in Figure 5.

5.3.2. Relative Relocations

We relocate earthquakes in boxes A-D (Figure 5) using the double-difference algorithm after cross-correlating P-wave arrivals using 0.3–0.6 s windows (e.g., Figure S9 in Supporting Information S1). The mean relative earthquake uncertainties of clusters are found using the SVD method (Table 1). The comparatively higher depth uncertainties for Box D are associated with the lateral velocity variations associated with the >5 km-thick sedimentary basins (e.g., Schofield et al., 2021). For Box A, the lack of stations to the NW as well as the lateral velocity variations associated with the ancient arc complex may have played a role in the relatively large horizontal and depth uncertainties in this region (Table 1 and Figure 5). The number of relocated earthquakes in each box is small in part owing to the large depth distribution of earthquakes in each area (0–25 km), and in part owing to the ~50 km station spacing of this reconnaissance array.

Earthquake clusters are concentrated in kinks or jogs in the axis of the rift zone where transfer faults link border faults. In the Aluma-Mali-Weyto sector, earthquakes along NNE-striking border faults are linked by seismically active NNW-striking faults. In boxes C and D, faults beneath Lake Turkana have been mapped from coarse seismic reflection coverage, and orientations are not well constrained. Our work shows a N350°-striking crustal-scale fault, as well as broad band of <10 km deep earthquakes across the Eliye kink.

The distribution of both the absolute and relocated earthquakes shows large differences in the breadth of the seismically active zone along the length of the rift. In southern Ethiopia, the combined breadth of the Usno-Aluma-Weyto-Chew Bahir and the Chamo-Segen-Ririba rifts (broadly rifted zone) is ~280 km. The zone of active seismic and geodetic strain narrows into the Omo-Turkana rift where in some parts, the thinnest crust (≤25 km) coincides with the doubly thinned crust (Mechie et al., 1994; Ogden et al., 2023) (Figure 1b).

5.4. Earthquake Depth Distribution

From the 748 relocated earthquakes, we produced a depth histogram overlain with cumulative seismic moment release using a crude assumption that $M_w = M_L$, in the absence of sufficient earthquakes with $M_L \geq 4$ to establish a scaling relationship and given that mb is approximately equal to Mw for earthquakes with mb ≤ 5 (Gasperini et al., 2013) (Figure 7). Not included is the teleseismically detected 3 May 2020, magnitude 5 M_w (4.5 M_L) event at a depth of 14 ± 1.5 km, which is grouped with teleseismically detected events. The pattern of seismic moment release will not change, but we acknowledge that the absolute values with depth will. We assume M_w = (logM_0–9.1)/1.5 in Nm (IASPEI, 2013). Despite the higher number of earthquakes at depths between 0 and 10 km as compared to 10–15 km, the seismic moment release values at 10–15 km are ~5 times greater than at 0–10 km, consistent with the decrease in *b*-value with depth (Figure S8 in Supporting Information S1). The 3

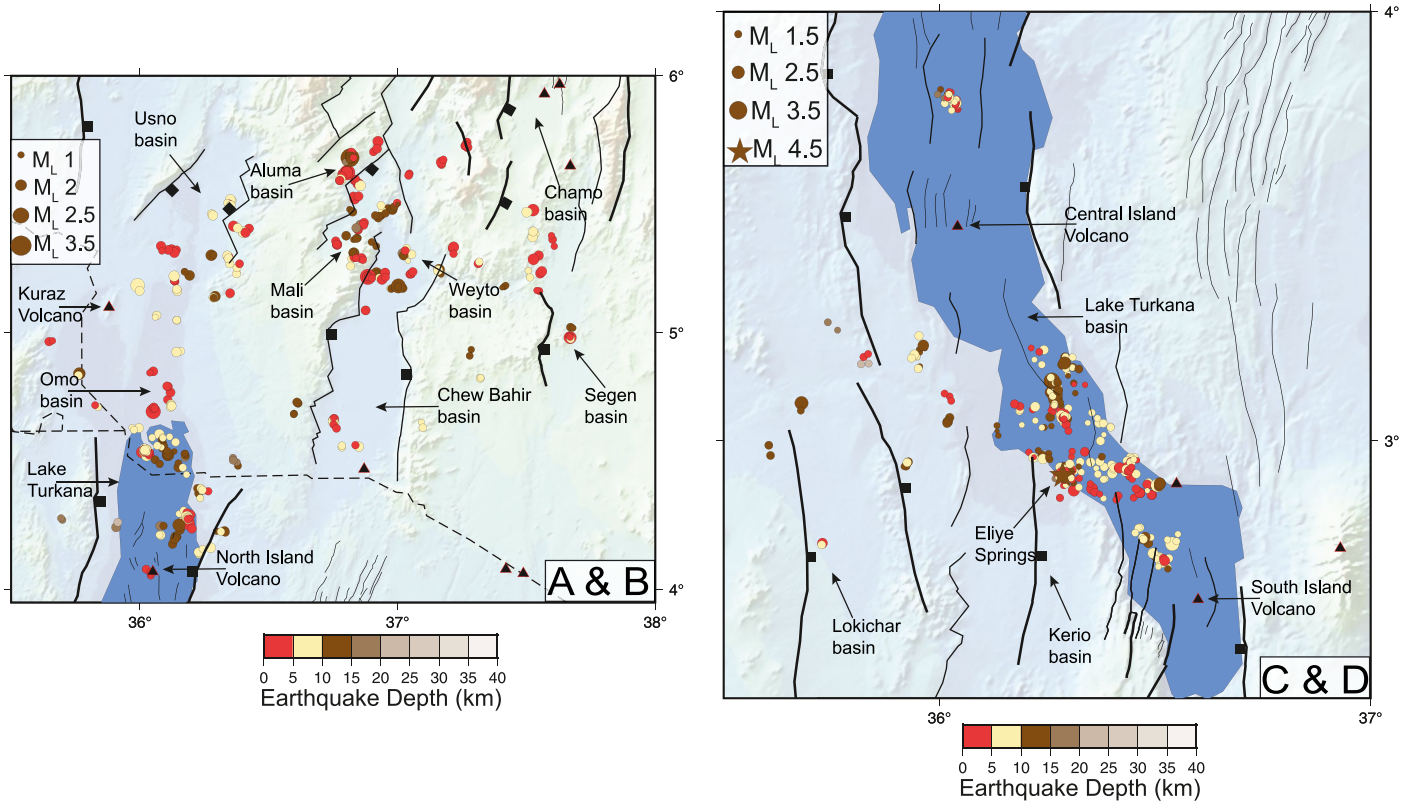

Figure 6. Relative locations of earthquake hypocenters relocated using double differencing located in zones A, B, C and D as shown in Figure 5. The brown star in (c) and (d) shows the relative location of the 3 May 2020, M_L 4.5 teleseismically detected earthquake in the study area. Overlaid are Cenozoic faults (black continuous lines) and Pleistocene-Recent eruptive centers (black triangles outlined in red).

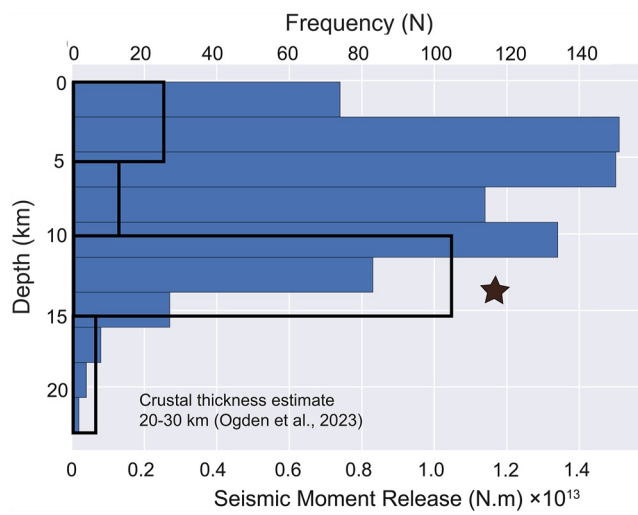

Figure 7. Histogram of hypocentral depths from 748 double-difference earthquake relocations from areas shown in Figure 6. Overlain in black are the seismic moment release values in Nm. We excluded the Mw 5 (M_L 4.5) earthquake at 14 ± 1.5 km (the brown star) as it obscures patterns. A significant increase in seismic moment release occurs at 10–15 km. The high seismic moment release values at depths of 10–15 km are surprising given the 20–28 km crustal depths in the study area (Ogden et al., 2023). The mid to lower crust accommodates a considerable amount of elastic strain in the Turkana Depression.

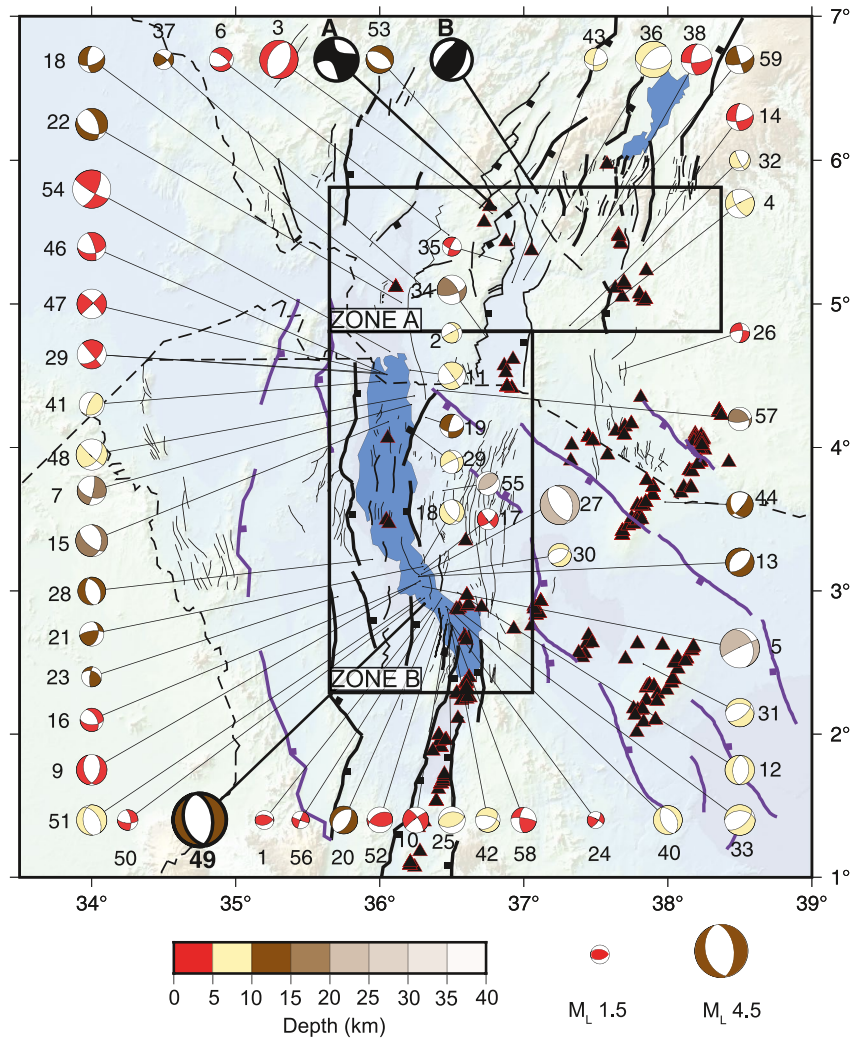

Figure 8. Focal mechanisms of 59 first motion focal mechanisms from the Turkana Rift Array to Investigate Lithospheric Structure (TRAILS) color-coded by depth, scaled by magnitude, and numbered as in Table S2 in Supporting Information S1. The teleseismically detected earthquake recorded by our array, Event 49, was analyzed using the Full Moment Tensor (FMT) inversion (Event 7b, Table S2 in Supporting Information S1 and Figure 10). Events A and B are FMT source mechanisms for the second and third largest earthquakes in our catalog with M_L 4 (Event A, Figure 9) and 3.8 (Event B, Figure S13 in Supporting Information S1) respectively (Figure 9). These two events at the northern limit of our array had azimuthal gaps >130° (Table S2 in Supporting Information S1). Stress inversions (Figures 11a and 11c) and Kostrov summation (Figures 12b and 12d–12f) are done in zones A and B, given the change in fault orientations, and geodetically determined opening directions (Figures 3 and 11). Overlain are the Mesozoic-Paleogene and Cenozoic fault structures in purple and black, respectively. Quaternary-Recent eruptive centers are in black triangles outlined in red.

May 2020, 5 M_w (4.5 M_L) teleseismically detected earthquake (14 ± 1.5 km) also occurred in this depth interval. The shallow earthquakes are associated with the extensive intra-basinal fault arrays and illustrated in representative cross-sections in the Discussion.

5.5. Earthquake Source Mechanisms

The source mechanism solutions comprise normal, strike-slip and reverse mechanisms with considerable obliquity (Figure 8). In the broadly distributed zone of deformation, the Usno-Aluma-Mali-Weyto rift, source mechanisms are predominantly normal and strike-slip. The <4 M_L earthquakes with strike-slip mechanisms have no surface expression of strike-slip faulting (Sullivan, 2023). The presence of strike-slip earthquakes of varying

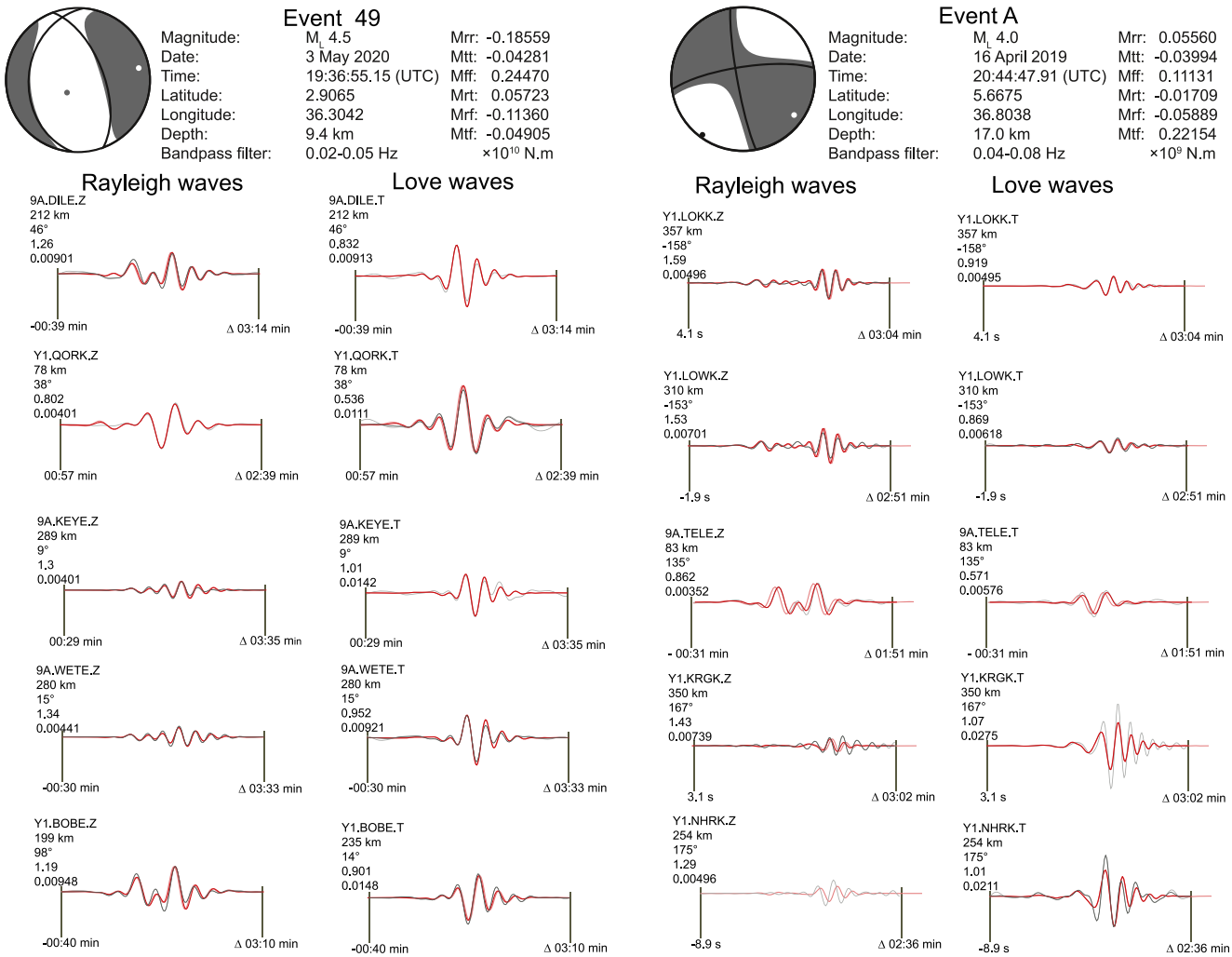

Figure 9. Full moment tensor inversion solutions (velocity seismograms) computed using the Grond package (Heimann et al., 2018) for the two events with $M_L \geq 4$ earthquakes recorded by TRAILS network including the 5 Mw (4.5 M_L) teleseismically detected earthquake. Event 49 is referenced in Figure 8 and Table S2 in Supporting Information S1 as Event 49, whereas Event A is as shown in Figure 8. P and T axes are denoted in gray and white, respectively. Five sample synthetic waveform fits (red) are plotted on top of the data (black) for each event. Light gray traces are untapered data waveforms and light red traces are unshifted waveforms. Information on the top left of each waveform includes the station name, station-to-receiver distance, azimuth, weighting factor, and relative residuals (See Supporting Information S1 for detailed explanations).

strikes and displacements argues against basin linkage by crustal-scale shear zones, but instead by arrays of sub-parallel NNE-striking normal faults linked by short NW-striking faults. Along the Turkana rift, there are a wide range of source mechanisms ranging from normal, strike slip and reverse. Many of these mechanisms correspond to sub-N-S border and intrabasinal faults and magmatic intrusions mapped at the surface and imaged by 2-D seismic reflection profiles (Corti et al., 2019; Dunkleman et al., 1989; Ebinger et al., 2000; Morley et al., 1992; Muirhead et al., 2022; Schofield et al., 2021).

We used Full Moment Tensor (FMT) inversion to model earthquakes with $M_L \geq 3.8$ recorded by our TRAILS array. These events include the magnitude 5 Mw (4.5 M_L) event on 3 May 2020, located SW of Lake Turkana rift basin (Event 49, Figure 8). The other two events are in the southern MER: the 4 M_L earthquake on 16 April 2019 (Event A, Figure 8) and the 3.83 M_L event on 12 May 2020 (Event B, Figure 8). Events A and B are not included in our 1st polarity motion focal mechanism catalog (Table S1 in Supporting Information S1) because they are close to the edge of our seismic array (Figure S1 in Supporting Information S1) and have azimuthal gaps

>130°. Our FMT source mechanism solution of Event 49 (Figure 8) is normal (Event 7b, Figure 10) with the nodal planes oriented in a sub-N-S trending strike consistent with the Global CMT solution (Event 7, Figure 10) that used an adaptive velocity model from the closest velocity profile from CRUST2 (Bassin et al., 2000), which is probably less representative of the velocity structure in the study area (Craig & Jackson, 2021) (Event 7a, Figure 10 and Table S2 in Supporting Information S1), and our local focal mechanism (Event 49, Figure 8 and Table S1 in Supporting Information S1). From our FMT results, the event has a centroid depth of 9.5 km that is within the depth uncertainties of the event's double-differenced relocated depth (10.8 ± 1.5 km) and less than the Global CMT (13.9 ± 4 km) depth. We attribute the depth differences to the lateral velocity anomalies from the deep (2–5 km) sedimentary basins along ray paths. Depth and source mechanism solutions' discrepancies across methods for Events A and B (Figure 8; Figures S12 and S13 in Supporting Information S1) are outlined in the Supporting Information S1. We interpret focal mechanisms with respect to representative cross-sections in the Discussion.

5.6. Rift Kinematics

From the 59 local source mechanisms that passed our selection criteria (Figure 8 and Table S2 in Supporting Information S1), 48 earthquakes had $M_L > 2.0$ and were used in our stress inversion analyses. We assumed that this new subset of earthquakes (48) represents tectonic stresses for use in the grid search stress inversion as well as Kostrov summation to determine the orientation of the principal stresses in the crust. Using seismicity, and new GNSS velocity profiles that supplement those of Knappe et al. (2020) we partition the study area into northern and southern zones based on the extent and style of deformation (Figures 7 and 9). In zone A, the deformation style is diffuse across an ∼280 km-wide seismically active zone spanning 3 rifts; in zone B, strain accommodation is localized to an ∼150 km-wide seismically active zone centered on the Turkana rift. Kostrov summation for the orientation of P- and T- axes and strain rates is done in a volumetric sense, where we assumed that the depths of the deforming zones are equal to the seismogenic layer thickness of 17 km (Figure 7; Figure S10 in Supporting Information S1). We tested the consistency of our inverted seismic strain rates in zones A and B by varying the zones' breadths using the extent of their seismic strain zones. We observe that regardless of the different breadth of deformation, the seismic strain rate in Zone B (Turkana rift) is about 7 times larger than that in zone A (broadly rifted zone in southern MER).

5.6.1. Local Earthquakes

We used the stress inversion method of Martinez-Garzon et al. (2014) to determine σ_1, σ_2, σ_3 and their uncertainties using 200 random bootstrap resamplings of input focal mechanism solutions. We consider analyses in two zones (Figures 8 and 10). In zone A, the stress field orientation of the T-axis (s_3) is 140° + 18°/−28° (Figure 11a), whereas in zone B, the orientation of the T-axis is 88° + 18°/−25° (Figure 11c). We also used Kostrov summation to constrain the orientation of the P- and T-axes and excluded the M_L 4.5 earthquake, which we consider with the teleseismically detected earthquakes. In zone A, the T-axis orientation is N138° + 20°/−15° (Figure 11b), whereas in zone B, the T-axis is N91° + 20°/−15° (Figure 11d). In zones A and B, the T-axis orientation estimates across methods are identical, within uncertainties.

5.6.2. Teleseismically Detected Earthquakes

Our 2-year array presents a temporally biased data set to consider plate-boundary strains. To expand the time intervals of the study's observations, we used teleseismically detected earthquake source mechanisms from the Global CMT project (e.g., Ekström et al., 2012) (Table S2 in Supporting Information S1). Additionally, we incorporated waveform modeling source parameter results for the Mw 5, 3 May 2020, teleseismically detected earthquake recorded by the local TRAILS array (Event 7b, Figure 10). We combined the source parameter results from these two independent analyses to address the 20–30 km horizontal uncertainties associated with the locations of the Global CMT results, and we incorporated adjusted depths with their corresponding waveform modeling results of Foster and Jackson (1998) and Craig and Jackson (2021).

Owing to the significant differences in source mechanisms in the northern and southern parts of the study area, and from inspection of source mechanisms, we see two families of mechanisms, WNW-ESE and E-W (Figure 10).

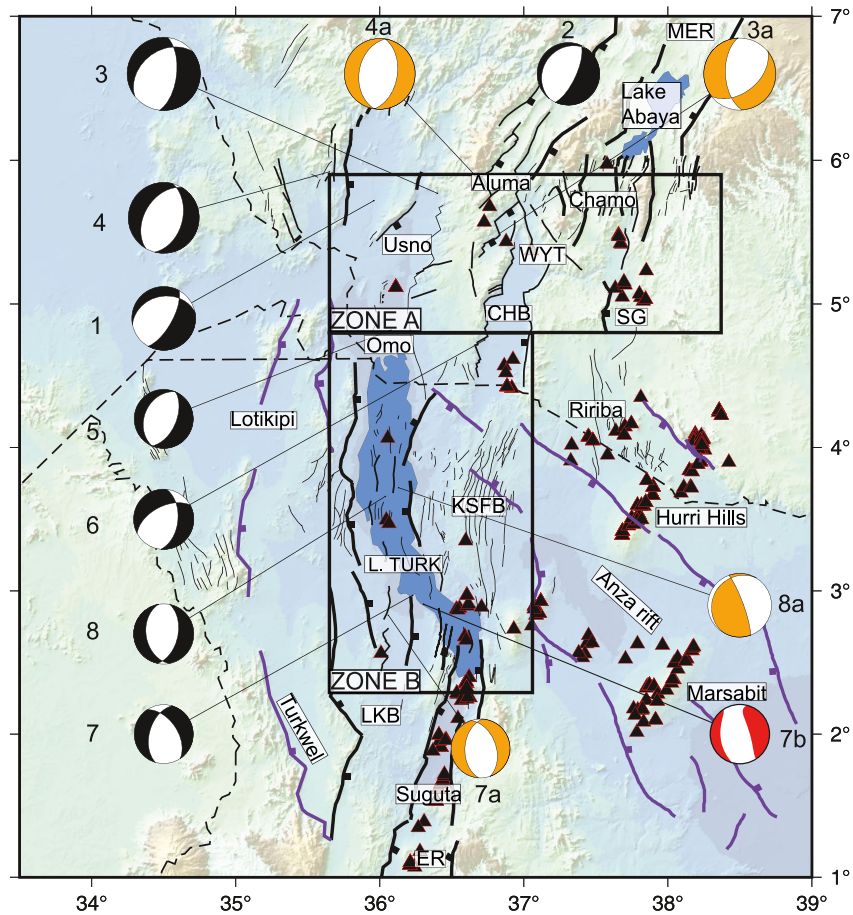

Figure 10. Source mechanisms for teleseismically detected earthquakes in the Turkana Depression from the Global CMT catalog between 1983 and 2022 (Table S3 in Supporting Information S1). Event location errors may be as large as 25 km (e.g., Weinstein et al., 2017); the GCMT location for the 3 May 2020, event (Event 7) differed by 11 km, but its depth is within our absolute location depth uncertainty estimates. Also plotted are the FMT source solutions for events with $M_L > 3.8$ in red, including the 5 Mw (4.5 M_L) teleseismically detected earthquake denoted as Event 7 (GCMT) with our FMT source mechanism solution as Event 7b in red and Craig and Jackson (2021) as Event 7a in orange. FMT solutions computed for pre-2019 teleseismically detected earthquakes in the region include Events 3a and 4a by Foster and Jackson (1998) and Event 8a (Craig & Jackson, 2021) in orange. Overlain are the Mesozoic-Paleogene and Cenozoic fault structures in purple and black respectively and Quaternary-Recent eruptive centers in black triangles. MER, WYT, CHB, SG, KSFB, L. TURK, LKB and ER are the Main Ethiopian Rift, Weyto, Chew Bahir, Segen, Kino Sogo, Lake Turkana, Lokichar and Eastern rift, respectively.

Although the number of teleseisms in each region is 4, we consider the same two boxes as in the local earthquake analyses (Figure 8). The resultant source parameter solutions of the teleseismically detected earthquakes were used in the Kostrov summation inversion to quantify the orientation of P- and T- axes and the strain rates in zones A and B (Figure 11a). We obtained the orientation of the T axis in zone A to be 115° + 20°/15°, whereas in zone B to be 88° + 18°/−25° (Figure 11a).

Comparing results between methods and between local and teleseismically detected earthquakes, all are identical, within uncertainties, which are <20° (Figure 11). The north to south variation in extension direction from WNW in the MER to E-W in the Eastern rift implied from the orientation of structures, therefore, is supported by our analyses. The near similarity of the principal stress orientations from stress inversion and Kostrov summation of local earthquakes with those from teleseismically detected earthquakes indicates that the local earthquakes recorded by the TRAILS temporary array are representative of the tectonic process in the region.

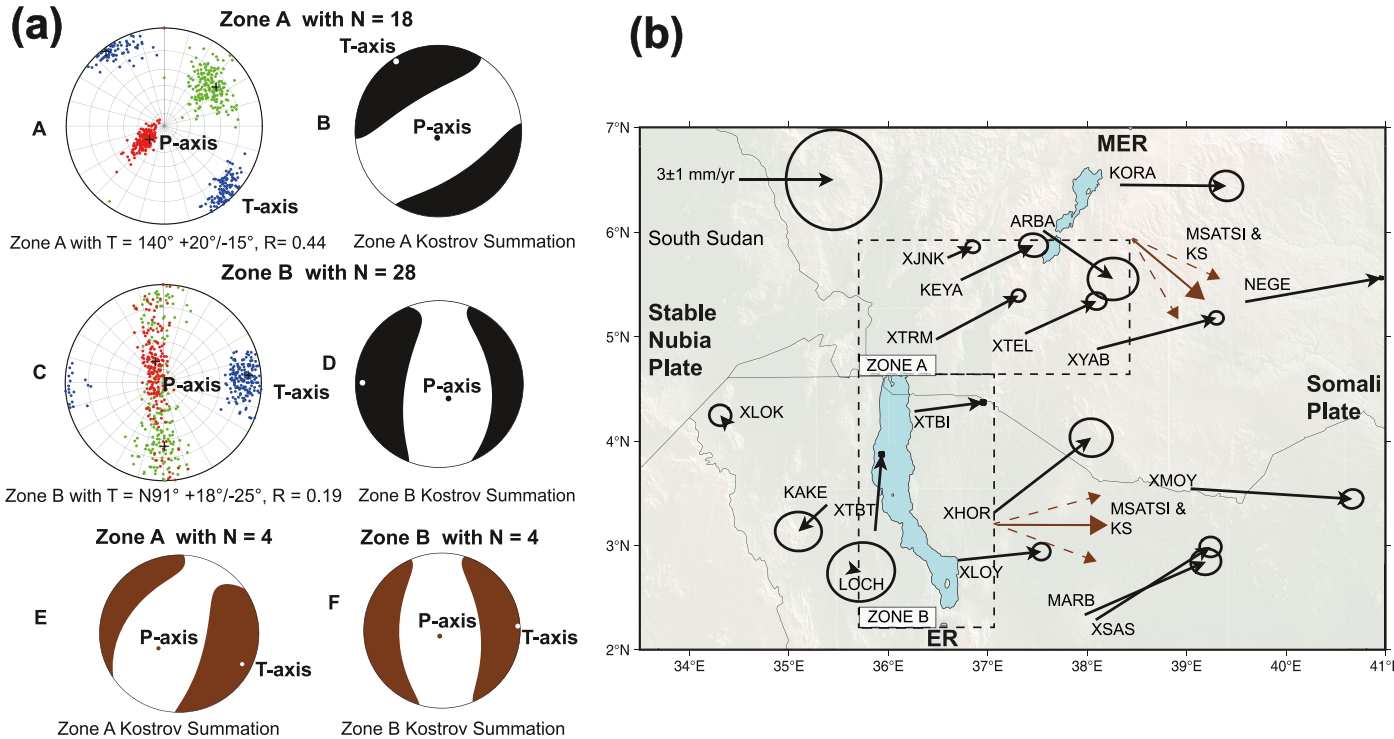

Figure 11. (a) Comparison of the stress inversion (a, c) using MSATSI (Martinez-Garzon et al., 2014) to determine the best fitting σ_1 (red), σ_2 (green) and σ_3 (blue) indicated by crosses and using solutions in Table S1 in Supporting Information S1. (b, d) Kostrov summation (KS) for local earthquakes from zones A and B in Figure 7. (e, f) Are Kostrov summation using the teleseisms, including the 2019 Mw 5.0 (M_L 4.5) earthquake. (b) Global Navigation Satellite System (GNSS) displacement vector solution (black arrows) using a fixed Nubia frame of reference with 95% confidence ellipse. Zones A and B, in black dotted boxes, are our two breadths of deformation, broadly and narrowly deforming zones, respectively. Solid and dotted brown arrows show the orientations of T-axes including uncertainty inverted from stress inversions as shown in (a). The similarities between the seismic inversions of the local earthquakes (2019–2021) and teleseismically detected earthquakes (1983–2022) indicate that our local source mechanism solutions are representative of the tectonic stress in the region. A comparison of our inverted T-axes orientations with the geodetic displacement vectors indicates that in zone B, the near eastward displacement of most GNSS stations are within the limits of uncertainty of the seismically inverted T-axis orientations contrary to what we observe in zone A. The discrepancy in GNSS and seismic-opening directions in zone A may indicate that areas northwest of Lake Turkana may not be stable, as was assumed in the GNSS solutions. The discrepancy in rift opening direction warrants further studies to explain this complex deformation zone.

6. Discussion

The new geodetic measurements of rift-opening velocities (see file in Supporting Information S1) combined with the spatial distribution of seismicity, fault kinematic information from earthquake source mechanisms and *b*-values provide new constraints on crustal strain patterns between the MER and ER. Crustal thickness variations determined from receiver function analyses (Ogden et al., 2023) and controlled source experiments (Mechie et al., 1994) provide information on time-averaged strains. Mantle tomographic imaging also provides insights into strain below the crust (Kounoudis et al., 2021, 2023). Our results, when integrated with the new TRAILS constraints on crustal thickness variations, the presence or absence of magmatic modification, and uppermost mantle velocity variations, enable us to evaluate the current models of linkage of the MER and ER, and to produce a revised modern plate boundary (Figure 12, digital file in the Supporting Information S1). These observations provide a common geodynamic framework for comparisons across and along the Turkana Depression and the MER and ER to the north and south, respectively. For ease of discussion, we construct three rift perpendicular lithospheric-scale profiles comparing seismicity and geodetic strain with zones of crust and mantle thinning and/or thermal anomalies (Figures 12 and 13).

6.1. Kinematics of Opening and Rift Linkage

We interpret the modern plate boundary between the Somali and Nubia plates as the zones of seismic and geodetic strain localization. In southern Ethiopia, the combined breadth of the Usno-Aluma-Mali-Weyto-Chew Bahir and

the Chamo-Segen-Ririba rifts (broadly rift zone) is ~280 km (Figures 5, 6, and 12). The zone of active seismic and geodetic strain narrows into the Omo-Turkana rift, where in some parts, the thinnest crust (≤25 km) is a consequence of superposed Mesozoic and Oligocene-Recent stretching (Mechie et al., 1994; Ogden et al., 2023). In this area, seismic and geodetic strain is largely focused across an ~150 km-wide region centered on the Lake Turkana rift, with no significant strain across the Quaternary-Recent volcanic field east of Lake Turkana or across the Kino Sogo and Ririba rift zones (Figures 5 and 12). Although the Chew Bahir-KSFB rift zone marks the shortest path of linkage between the MER and the Suguta rift, the Lake Turkana rift zone ~50 km to the west appears to be the locus of strain (Figures 5, 12, and 13).

We create representative cross sections to illustrate the variations in seismicity and kinematics with respect to rift structures (Figure 13). The dip angle was constrained by projecting faults imaged by seismic reflection profiles, assuming a fault dip of 50° (e.g., Dunkleman et al., 1989; Muirhead et al., 2022; Schofield et al., 2021) (Figure 13). A comparison of the projected faults, seismicity, and focal mechanisms to our 2-D crustal cross sections (Profiles A-A′, B-B′, and C-C′, Figure 13) demonstrate along-strike variation in the distribution of seismicity and fault kinematics.

Our analysis of well-located earthquakes indicate border and intra-basinal faults, and localized magma intrusions are accommodating active extension along the active plate boundary to depths of 15–20 km, arguing against detachment faults soling at 10 km in earlier interpretations (e.g., Morley et al., 1992, 1999). Moving from north to south, Profiles A-A′ and B-B′ sample the broadly rifted zone (zone A, Figure 12). The broad zone of deformation has NW and NNE dominant fault strike orientations having normal and strike-slip focal mechanisms with considerable obliquity (Profiles A-A′ and B-B′, Figure 13). Further south, the ER links with the Turkana Depression at the Eliye kink (Figures 5 and 6), which is a complex damage zone that has (a) deforming en echelon normal faults linked with relay ramp interaction zones projected to the normal and strike-slip source mechanisms, respectively (Figure 13; Profile C-C′) (Sullivan, 2023) and (b) active localized magma intrusions imaged by reflection imaging (Dunkleman et al., 1989; Muirhead et al., 2022; Schofield et al., 2021). One of these intrusions corresponds, within pre-GNSS navigation uncertainties in the seismic reflection data, with the observed pipe-like cluster of seismicity along Profile C-C′ (Figure 13). Mid-lower crust normal and upper crust strike-slip focal mechanisms (Profile C-C′, Figure 13) in this cluster are observed in other dike and sill complexes (e.g., Oliva et al., 2019). The 3 May 2020, Mw 5.0 (4.5 M_L) earthquake occurred along a projection of the Kerio border fault surface trace to 15 km depth; its aftershocks outline the activated fault array in this heavily faulted zone (Profile C-C′, Figure 13).

Seismic strain observations reveal a significant change in the rift-opening direction from N115° + 20°/−15° in the southern MER and broadly rifted zone to N87° + 18°/−25° in the narrow deforming Omo-Turkana rift, and southward along the Eastern rift (Figure 11). The differences in rift-opening directions imply fault block rotations along vertical axes in this zone, but our seismic and geodetic arrays were too coarse to quantify. The change in rift-opening direction coincides with the broadly rifted zone, which in turn overlies a ribbon of seismically fast, strong mantle lithosphere associated with a Proterozoic Island arc terrane (Kounoudis et al., 2021, 2023) (Figure 12a, Zone A). The unusual breadth of the Turkana section of the East African rift zone, therefore, may in part be a consequence of the stronger, colder lithosphere: small strains are distributed across a broad zone, as compared to larger strains across narrow zones to the north (MER) and south (ER).

Our results argue against the linkage of the MER, ER and Western rift in the Turkana Depression and contradict models for the reactivation of the Aswa shear zone in the study area (e.g., Chorowicz, 2005; Katumwehe et al., 2016). The lack of seismic and geodetic data northwest of the Turkana rift (Knappe et al., 2020) allows for a possible connection northwest of the study area. Additionally, at mantle depths, there is no evidence of low mantle wavespeed anomalies connecting the ER to the Western rift (Kounoudis et al., 2021); we have no data to the NW in South Sudan where non-rigid behavior may explain the discrepancy between geodetic and seismic-opening directions in the broadly rifted zone in southern MER (Zone A, Figure 11b). Likewise, our study shows no evidence of reactivation of the NW-striking Mesozoic rift structures in the Anza graben or NW-striking Cretaceous-Paleogene structures in the Lotikipi region (Figures 5 and 12). The observed zone of active deformation is much smaller than that proposed by numerical models of propagating rift zones (e.g., Brune et al., 2017). Corti et al. (2019) suggest that linkage between the MER and the ER was through the evolution of two overlapping and disconnected rifts into a single oblique rift. However, our results indicate that the westward deflection of the modern-day plate boundary in the southern MER coincides with multiple lithospheric heterogeneities: the NW-trending accreted Paleoproterozoic-age terrane with strong and refractory mantle lithosphere (Kounoudis et al., 2021, 2023), and the Mesozoic Anza rift, whose crust-to-mantle lithospheric ratio at the onset of Miocene-Recent rifting was lower

Table 2
Strain Rates Determined From Teleseismically Detected Earthquakes (Table S2 in Supporting Information S1) and Global Navigation Satellite System Stations Located in Zones A and B (Figure 12)

Region	S-strain rate (s^{-1})	S-strain rate (yr^{-1})	G-strain rate (yr^{-1})	T-axis local EQs (MSATSI)	T-axis local EQs (KS)	T-axis TDEs (KS)
Zone A	6.2×10^{-17}	1.9×10^{-9}	7.4×10^{-8}	140°	138°	115°
				+20°/−15°	+20°/−15°	+20°/−15°
Zone B	9.5×10^{-18}	2.9×10^{-10}	8.5×10^{-8}	88°	91°	87°
				+18°/−25°	+20°/−15°	+20°/−15°

Note. S- and G- denote seismic and geodetic, respectively. T-axis orientation deduced from local earthquakes (EQs) (Figure 8) and teleseismically detected earthquakes (TDEs) (Figure 10) from stress inversion and Kostrov summation. KS is Kostrov summation.

than surrounding areas (Ogden et al., 2023). Lithospheric heterogeneities appear to control the distribution of crustal deformation, and hence the location of the modern-day plate boundary (Figure 12).

6.2. Differences Between Seismic and Geodetic Strain Rates

Differences between the seismic and geodetic strain rates provide a means to quantify aseismic deformation within weakly magmatic rifts (e.g., Zheng et al., 2020). Aseismic deformation may occur co-seismically, post-seismically and inter-seismically through creep and magma intrusion processes (e.g., Lindenfeld et al., 2012; Zheng et al., 2020). In zones A and B (Figure 10), Kostrov summation of teleseismically detected earthquake source mechanisms indicate seismic strain rates of 6.2×10^{-17} s^{-1} or 1.9×10^{-9} yr^{-1} and 9.5×10^{-18} s^{-1} or 2.9×10^{-10} yr^{-1}, respectively. However, geodetic strain rates in zones A and B are 7.4×10^{-8} yr^{-1} and 8.5×10^{-8} yr^{-1}, respectively (Table 2). Looking at the seismic strain rates inverted from Kostrov summation of the teleseismically detected events, we observe that in the diffuse zone of deformation (~280 km wide, zone A), the seismic strain rate is ~7 times greater than in the narrow deforming zone (~150 km wide, zone B).

Geodetic strain rates across the broadly rifted zone and the more narrowly deforming Omo-Turkana rift are more than a factor of 25 greater than seismic estimates indicating that aseismic processes accommodate most of the strain. However, the largest seismic and geodetic strain rate discrepancy (30 times smaller) is along the relatively narrowly deforming, magmatically active Omo-Turkana rift (Table 2), suggesting that magma intrusion accounts for some of the aseismic deformation. In the South Island area where the Turkana rift links to the Suguta rift, Muirhead et al. (2022) argue that 85% of the <1 Ma extension is accommodated within the axial magmatic zone, and our results suggest that this relation holds for the length of the Turkana rift. The seismic-geodetic strain discrepancy in the Turkana rift is comparable to that of the magmatic North Tanzania Divergence zone (Weinstein et al., 2017). Similar geodetic to seismic discrepancies in the broadly deforming zone are observed in the cratonic and magma-poor South Tanganyika rift (Lavayssière et al., 2019) and the Malawi rift (Ebinger et al., 2019). Thus, aseismic deformation appears to be a widespread feature of extension across the EARS, with the largest discrepancy associated with zones of active magmatism.

6.3. Lower Crustal Earthquakes

Earthquakes occur at depths of 15–22 km in 20–30 km-thick crust thinned during multiple rifting episodes (Ogden et al., 2023) (Figure 7). Lower crustal earthquakes occur in areas unaffected by Holocene magmatism, as well as along a pipe-like cluster of earthquakes between Central and North Island volcanoes in Lake Turkana (Profile C-C′, Figure 13). Several models have been proposed to explain the mechanism of lower crustal earthquakes: brittle deformation of a cool dry, mafic lower crust in areas lacking the surface expression of magmatism (e.g., Albaric et al., 2009; Lavayssière et al., 2019), and magmatic intrusions which may release volatiles that increase pore pressures causing small magnitude earthquakes (e.g., Lindenfeld et al., 2012; Muluneh et al., 2021; Weinstein et al., 2017). Lower crustal xenoliths from Cenozoic volcanoes in the Pan-African orogenic belt indicate a dry and mafic lower crust that may be granulitic in composition (e.g., Chin, 2018), perhaps explaining the deep seismicity in the broadly deforming zone.

6.4. Strain and Lithospheric Heterogeneities

The lithospheric-scale cross sections enable us to address two questions: (a) Do zones of active mantle lithospheric extension and/or melt accumulation coincide with zones of crustal thinning, active crustal

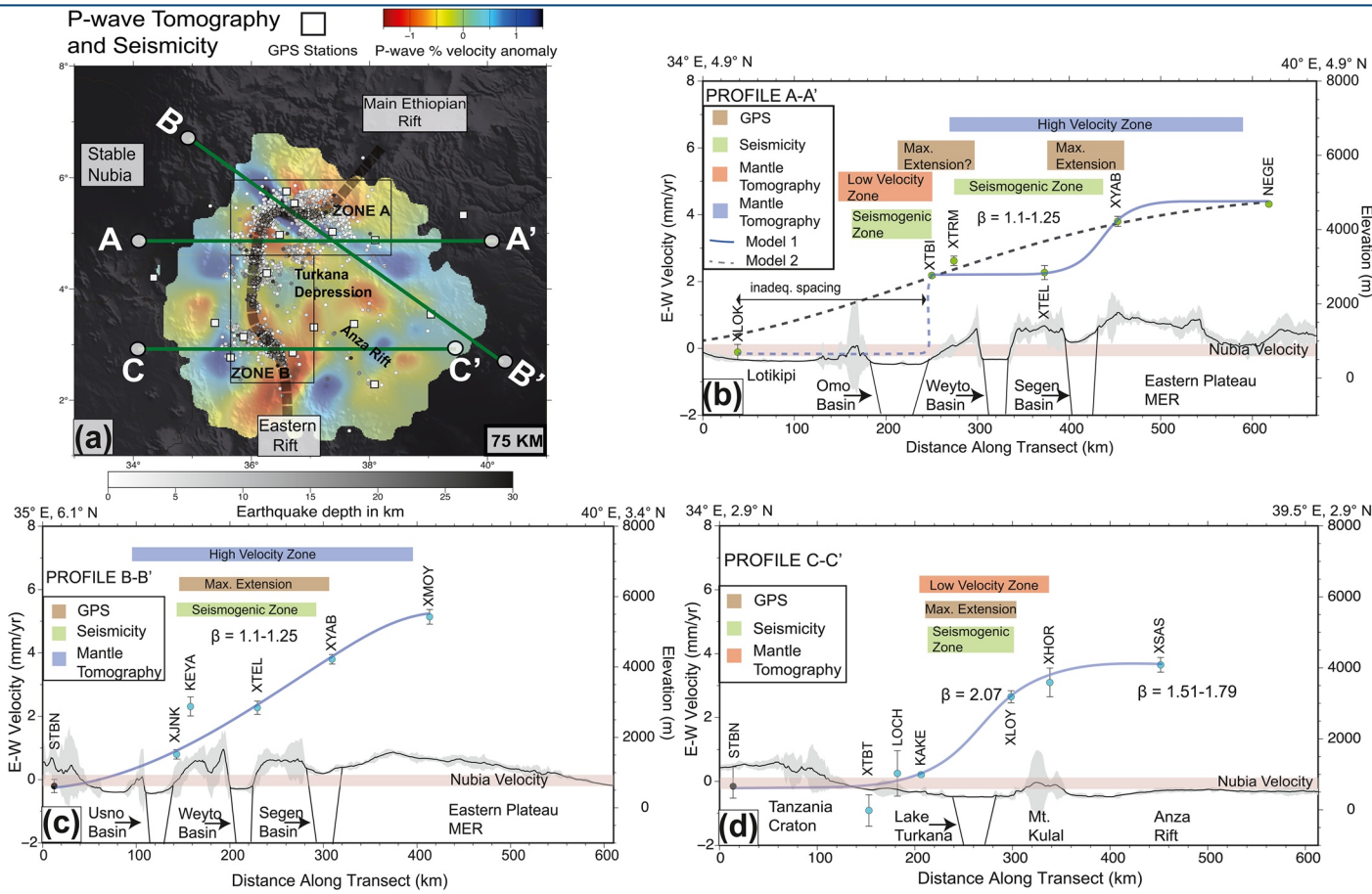

Figure 12. (a) Seismicity and Global Navigation Satellite System (GNSS) stations overlying the 75 km P-wave tomography slice from Kounoudis et al. (2021) comparing low velocity zones interpreted as mantle lithospheric thin zones or melt-infiltrated lithosphere (red) and the NW-SE high P-wave velocity ribbon interpreted as a pre-existing heterogeneity. The unobscured spatial distribution of 75 km-deep mantle velocity anomalies is in the supplementary material, Figure S14 in Supporting Information S1. The gray dotted line is the modern-day plate boundary constrained from the synthesis of our seismic and geodetic results. Sigmoid fits to GNSS data are shown by bold blue curves. (b) Profile A-A′ model 2 sigmoid fit has pinned point at stable Nubia plate, ~100 km away from XLOK station. Locations of the maximum strain (inflection points) along the profiles are 435 ± 18 km (profile A-A′, model 1), 239 ± 14 km (profile A-A′, model 2), 265 ± 23 km (profile B-B′, (c)), and 267 ± 12 km (profile C-C′, (d)). Total (time averaged) crustal stretching factors (β) from Ogden et al. (2023). Low velocity anomalies in the upper mantle are overlain by crustal with $\beta = 2.07$ (Profiles C-C′), whereas zones with higher velocity upper mantle have a diffuse style of active deformation with relatively low crustal stretching factors of $\beta = 1.10$–1.25 (Profiles A-A′ and B-B′). In the diffuse zone of deformation, we suggest a strong deforming block between higher strain zones (profile A-A′, models 1 and 2). STBN is pinned point on the stable Nubia plate.

deformation, and magmatism? And (b) What are the roles of pre-existing crust and mantle heterogeneities on the localization of Oligocene-Recent rifting?

We assume that (a) the active rift zones imaged at mantle lithosphere depths as slow wavespeed anomalies are one or a combination of mantle lithosphere thinning or melt intruded lithosphere (Kounoudis et al., 2021) and (b) the high wavespeed band, interpreted as strong lithosphere in southern Ethiopia, is part of the mantle lithosphere (Kounoudis et al., 2021, 2023). Ogden et al. (2023) argued that zones with crustal stretching factors $\beta > 1.9$ have doubly thinned crust; Cretaceous-Paleogene and Miocene-Recent rifting as imaged in some parts adjacent and along the Lake Turkana rift basin. Chew Bahir-Weyto rift (outside the Mesozoic rift) has $\beta = 1.35$–1.60 amounting to the largest Miocene-Recent rifting we detect, but thinner crust could underlie Lake Turkana, the locus of subsidence and axial volcanoes (Ogden et al., 2023). The comparatively low average crustal Vp/Vs ratios of ≤1.75 argue against widespread and significant magma intrusion.

Zones with crust ≤25 km underlain by upper mantle low velocity anomalies along modern plate boundary are interpreted as zones of mantle lithosphere thinning, and/or melt-infiltrated lithosphere (Kounoudis et al., 2021) (Profiles C-C′ and A-A′, Figures 12 and 13). The zones with most modest and widely distributed crustal strain are underlain by a high P-wave velocity anomaly at 50–100 km depths, which is interpreted as a cold and strong Pan-African accreted terrane (Kounoudis et al., 2021, 2023). Kounoudis et al. (2021) proposed that

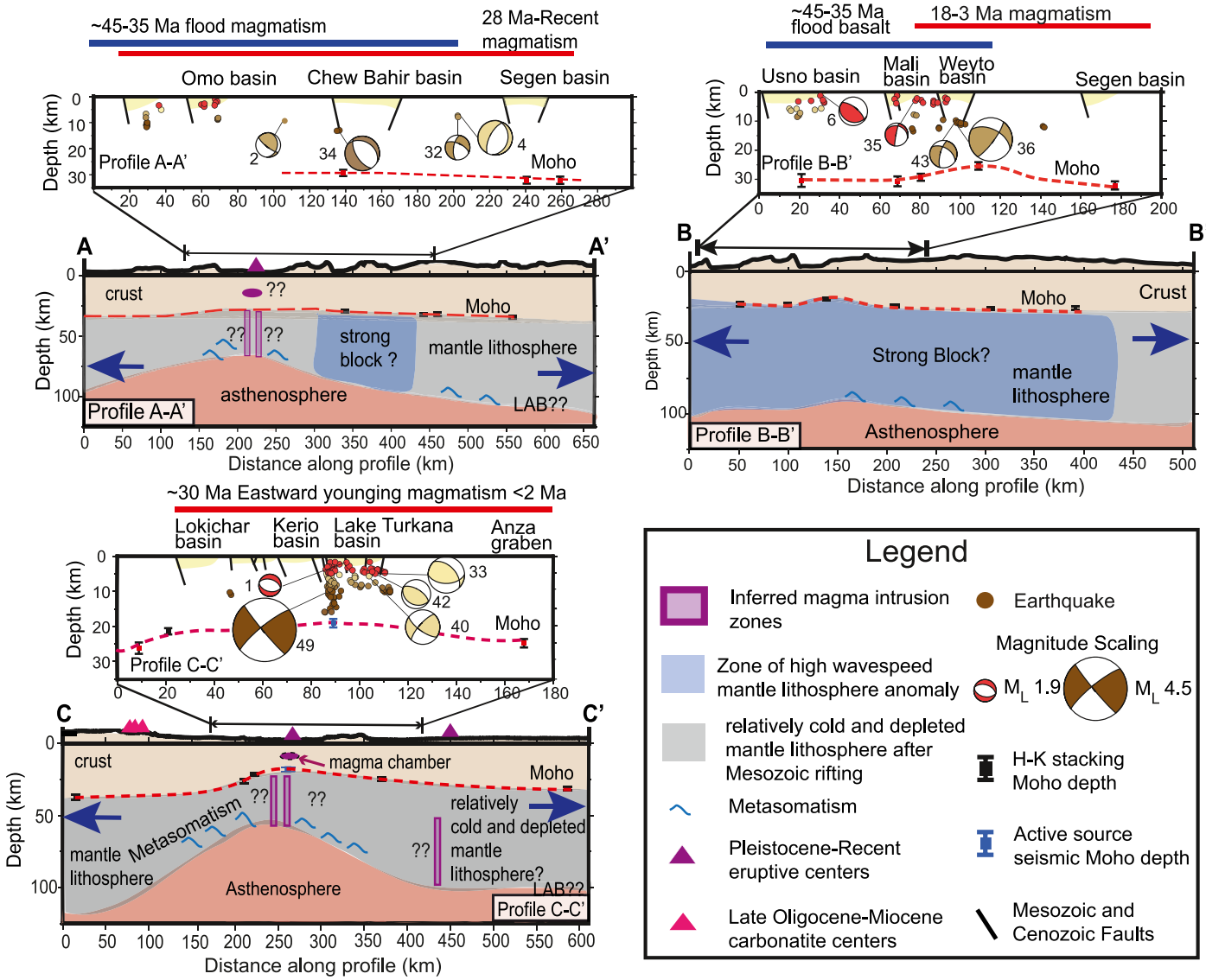

Figure 13. Schematic diagrams along profiles A-A′, B-B′, and C-C′ in Figure 12 highlight plate scale heterogeneity and deformation in the Turkana Depression. Magmatism shown with horizontal lines are color-coded by age (after Global Volcanism Program, 2013; Muirhead et al., 2020; Schofield et al., 2021; Steiner et al., 2022, Sullivan, 2023). Double-difference earthquake locations and focal mechanisms, within ±5 km of each profile, are projected to the crustal-scale structural cross sections. Earthquakes with magnitude less than M_L 2–2.5 may not represent tectonic strains. Moho depth estimates from receiver function measurements (black; Ogden et al., 2023) and active source seismology along the Turkana rift (blue; Mechie et al., 1994). The dashed red line approximates Moho. Seismicity clusters along steep border and intra-basinal faults, and local magma intrusions. Lithospheric mantle wavespeed information is from Kounoudis et al. (2021).

the NW-striking pre-existing terrane governed strain localization during both Mesozoic and Cenozoic rifting episodes. Along this accreted terrane, there is largely no Quaternary-Recent eruptive center (Figure S14 in Supporting Information S1), consistent with the refractory mantle interpretation.

Pre-existing Mesozoic rift structures are rarely exploited, and steep rift faults crosscut shallow dipping shear zones within the Pan-African orogen. Precisely relocated earthquakes lie along projections of border and transfer faults to lower crustal depths, arguing against shallow detachments. The active rift boundary appears to circumnavigate the pre-existing Anza graben, which may have been stronger than the surrounding crust in Oligocene time, owing to the larger ratio of strong lithospheric mantle to weak crust (Ogden et al., 2023). Based on these clear patterns, we postulate that mantle lithosphere heterogeneities play a major role in strain localization, faulting, crustal thinning, and possibly localization of magmatism, consistent with the mantle upwelling driving mechanism for rifting.

The role of magmatism in strain patterns is less clear. Along the length of the Omo-Turkana rift, eruptive centers aligned along the central rift zone correlate with slow velocity anomalies from 75 to 100 km subsurface (Kounoudis et al., 2021). At depths >200 km, the largest amplitude slow wavespeed anomalies underlie the largely unfaulted and aseismic Holocene eruptive centers east of Lake Turkana rift (Kounoudis et al., 2021), suggesting that the 25 Ma-Recent eastward migration of the depocenter may be linked to dynamic mantle processes (Morley, 1994). Our synthesis argues against the interpretation of Franceschini et al. (2020) that eruptive centers east of Lake Turkana reactivate inherited Precambrian and Mesozoic crustal structures: the deeper mantle melt zones instead appear to drive the location of magmatism.

7. Conclusions

We used the 2019–2021 TRAILS seismic array and two permanent seismic stations to identify the seismic strain zones in the southern Main Ethiopian rift (MER), Turkana Depression, and northern Eastern rift (ER). Our local seismicity catalog was relocated using a new 1-D velocity model with horizontal uncertainties <3.2 km, and <2.1 km in depth. Relative earthquake locations determined using cluster analyses have location accuracies ≤1.5 km. Using a new magnitude scaling relation with station corrections, the 1716 earthquakes are $1.0 \leq M_L \leq 4.5$ M_L and have a b-value of 1.22 ± 0.06 with a magnitude of completeness of 1.78. The seismogenic layer thickness is ∼17 km, consistent with the range of depths from our full-moment tensor (FMT) analyses, and with the depths of teleseismically detected earthquakes. Using stress inversion of 59 first motion source mechanisms and 3 FMTs, we observe a rotation in extension direction from N115° + 20°/−15° in the southern MER and broadly rifted (rift stepover) zone to N87° + 18°/−25° in the zones of active extension spanning the Turkana Depression and Eastern rift, consistent with variations in fault strike orientations. GNSS data used was acquired from 20 continuous and campaign GNSS stations spanning the region. Most of our GNSS displacement vectors in the narrowly deforming Omo-Turkana rift have near eastward extension direction consistent with our seismic inversions of the T-axis except for the broadly rifted zone. The ∼30° discrepancy in rift opening direction in this broad zone may indicate incorrect assumptions regarding stable Nubia in South Sudan. Maximum seismic and geodetic strains spatially correlate. Comparison of seismic and geodetic strain rates indicates that most of the rift opening occurs aseismically. The Turkana rift with active volcanoes appears to have a significantly larger component of aseismic deformation than the broadly rifted zone, suggesting that magma intrusion may contribute to extension over annual cycles.

Linkage of the Main Ethiopian and Eastern rifts is achieved through a zone of three, right stepping en echelon basins, creating a deflection of the active plate boundary north of the Turkana Depression. The broad zone of distributed strain coincides with a zone seismically fast, strong, and refractory upper mantle linked to a Proterozoic accreted terrane. The diffuse strain, the small amounts of crustal thinning ($\beta = 1.10$–1.25), and the large lack of Quaternary eruptive centers suggest that mantle heterogeneity may explain the lack of strain localization and magmatism in the stepover zone. During the inception of the most recent episode of rifting at ∼27 Ma, the large ratio of strong lithospheric mantle to weak crust of the Mesozoic Anza rift may have deflected Miocene-Recent stretching to areas with thicker crust. In the deflected Miocene-Recent stretching, west of the Anza rift, the active plate boundary narrows along the Omo-Turkana rift with sub-N-S border and intrabasinal faults, Pleistocene eruptive centers, and seismically imaged magma intrusions along the rift axis. This narrowly deforming Omo-Turkana rift has high amounts of crustal thinning ($\beta > 1.9$) and high aseismic to seismic strain rates (25 times greater) underlying a zone of seismically slow mantle velocity inferred as zones of mantle lithosphere thinning and/or melt-infiltrated plate. Further south, the narrowly deforming Omo-Turkana rift links with the ER through deforming en echelon normal faults linked with relay ramp interaction zones and active localized magma intrusions. The correlation of crustal strain patterns to mantle lithosphere heterogeneities implies that the mantle lithosphere exerts some control on the locus of crustal deformation; the location and linkage of faults, crustal thinning, and localized magmatic intrusions are consequences of heterogenous lithosphere.

Data Availability Statement

Seismic data obtained from the TRAILS project are archived at IRIS under two network codes Y1 (Ebinger, 2018) and 6R (Bastow, 2019). Data from an additional permanent seismic station, LODK, were sourced from OREFUS (https://www.orfeus-eu.org). Further north in the study area, in southern MER, we used seismic data from temporary seismic station, ARGA, as part of the Lake Abaya project (Ogden et al., 2021). Campaign and continuous geodetic data are archived at UNAVCO (Bendick et al., 2007, 2017).

Acknowledgments

We thank reviewers A. Koptev and D. B. Keir for their constructive comments. We acknowledge the collaborative efforts of the University of Nairobi, Dedan Kimathi University, and Addis Ababa University, our local university partners in Kenya and Ethiopia, for helping establish the Turkana Rift Array to Investigate Lithospheric Structure (TRAILS) network. Notable are Emma Chambers and the graduate students from local universities: S. Mwangi, M. Karanja, M. Wanyaga, B. Onguso and S. Alemayehu for assisting in the installation and servicing of the TRAILS seismic and geodetic networks. C. Ebinger and M. Musila acknowledge the support of the National Science Foundation Grant 1824417. R. Bendick, E. Knappe and M. Perry acknowledge support from the National Science Foundation Grant 1824199, 1824417, 17277277, and 1551823. I. Bastow, C. Ogden and R. Kounoudis acknowledge support from National Environment Research Council Grant NE/S014136/1. R. Kounoudis also acknowledges support from the Imperial College President's PhD Scholarship. F. Illsley-Kemp is supported by the ECLIPSE program, which is funded by the New Zealand Ministry of Business, Innovation and Employment (MBIE), the New Zealand Earthquake Commission Programme in Earthquake Seismology and Tectonic Geodesy at Victoria University of Wellington, and by the Marsden Fund of the Royal Society of New Zealand (Grant VUW2109). For the purpose of open access, the author has applied a Creative Commons Attribution (CC BY) license to any Author Accepted Manuscript (AAM) version arising.

References

Albaric, J., Déverchère, J., Petit, C., Perrot, J., & Le Gall, B. (2009). Crustal rheology and depth distribution of earthquakes: Insights from the central and southern East African Rift System. *Tectonophysics*, *468*(1–4), 28–41. https://doi.org/10.1016/j.tecto.2008.05.021

Altamimi, Z., Métivier, L., Rebischung, P., Rouby, H., & Collilieux, X. (2017). ITRF2014 plate motion model. *Geophysical Journal International*, *209*(3), 1906–1912. https://doi.org/10.1093/gji/ggx136

Altamimi, Z., Rebischung, P., Métivier, L., & Collilieux, X. (2016). ITRF2014: A new release of the international terrestrial reference frame modeling nonlinear station motions. *Journal of Geophysical Research: Solid Earth*, *121*(8), 6109–6131. https://doi.org/10.1002/2016JB013098

Bassin, C., Laske, G., & Masters, G. (2000). The current limits of resolution for surface wave tomography in North America. *EOS Transactions AGU*, *81*, F897.

Bastow, I. D. (2019). Turkana rift arrays to investigate lithospheric strains—UK component [Dataset]. International Federation of Digital Seismograph Networks. https://doi.org/10.7914/SN/6R_2019

Bendick, R., Knappe, E., Bastow, I., Ebinger, C. J., Mariita, N., Kianji, & G., & Nengo, I. (2017). Turkana GPS network. The GAGE facility operated by UNAVCO, Inc., GPS/GNSS observations (aggregation of multiple datasets). https://doi.org/10.7283/WF02-PP16

Bendick, R., Reilinger, R. E., & Knappe, E. (2007). *Ethiopia tectonics GPS network*. The GAGE facility operated by UNAVCO. Inc., GPS/GNSS Observations (Aggregation of Multiple Datasets). https://doi.org/10.7283/KE8V-G690

Benoit, M. H., Nyblade, A. A., & Pasyanos, M. E. (2006). Crusta l thinning between the Ethiopian and East African plateaus from modeling Rayleigh wave dispersion. *Geophysical Research Letters*, *33*(13), L13301. https://doi.org/10.1029/2006GL025687

Birhanu, Y., Bendick, R., Fisseha, S., Lewi, E., Floyd, M., King, R., & Reilinger, R. (2016). GPS constraints on broad scale extension in the Ethiopian Highlands and Main Ethiopian Rift. *Geophysical Research Letters*, *43*(13), 6844–6851. https://doi.org/10.1002/2016GL069890

Boone, S. C. (2018). A low-temperature thermochronology investigation of the Turkana depression: Implications for the development of the East African rift system (PhD thesis). University of Melbourne.

Boyce, A., Kounoudis, R., Bastow, I., Cottaar, S., Ebinger, C., & Ogden, C. (2023). Mantle wavespeed and discontinuity structure below East Africa: Implications for Cenozoic hotspot tectonism and the development of the Turkana Depression. https://doi.org/10.17863/CAM.99070

Bruhn, R. L., Brown, F. H., Gathogo, P. N., & Haileab, B. (2011). Pliocene volcano-Tectonics and paleogeography of the Turkana basin, Kenya and Ethiopia. *Journal of African Earth Sciences*, *59*(2–3), 295–312. https://doi.org/10.1016/j.jafrearsci.2010.12.002

Brune, S., Corti, G., & Ranalli, G. (2017). Controls of inherited lithospheric heterogeneity on rift linkage: Numerical and analog models of interaction between the Kenyan and Ethiopian rifts across the Turkana Depression. *Tectonics*, *36*(9), 1767–1786. https://doi.org/10.1002/2017TC004739

Buck, W. R. (2004). Consequences of asthenospheric variability on continental rifting. In *Rheology and deformation of the lithosphere at continental margins* (pp. 1–30). Columbia University Press. https://doi.org/10.7312/karn12738-002

Chang, S. J., Kendall, E., Davaille, A., & Ferreira, A. M. G. (2020). The evolution of mantle plumes in East Africa. *Journal of Geophysical Research: Solid Earth*, *125*(12), e2020JB019929. https://doi.org/10.1029/2020jb019929

Chang, S. J., & Van der Lee, S. (2011). Mantle plumes and associated flow beneath Arabia and East Africa. *Earth and Planetary Science Letters*, *302*(3–4), 448–454. https://doi.org/10.1016/j.epsl.2010.12.050

Chin, E. J. (2018). Deep crustal cumulates reflect patterns of continental rift volcanism beneath Tanzania. *Contributions to Mineralogy and Petrology*, *173*(10), 1–22. https://doi.org/10.1007/s00410-018-1512-z

Chorowicz, J. (2005). The East African rift system. *Journal of African Earth Sciences*, *43*(1–3), 379–410. https://doi.org/10.1016/j.jafrearsci.2005.07.019

Corti, G., Cioni, R., Franceschini, Z., Sani, F., Scaillet, S., Molin, P., et al. (2019). Aborted propagation of the Ethiopian rift caused by linkage with the Kenyan rift. *Nature Communications*, *10*(1), 1–11. https://doi.org/10.1038/s41467-019-09335-2

Cote, S., Kingston, J., Deino, A., Winkler, A., Kityo, R., & MacLatchy, L. (2018). Evidence for rapid faunal change in the early Miocene of East Africa based on revised biostratigraphic and radiometric dating of Bukwa, Uganda. *Journal of Human Evolution*, *116*, 95–107. https://doi.org/10.1016/j.jhevol.2017.12.001

Craig, T. J., & Jackson, J. A. (2021). Variations in the seismogenic thickness of East Africa. *Journal of Geophysical Research: Solid Earth*, *126*(3), e2020JB020754. https://doi.org/10.1029/2020JB020754

Davidson, A. (1983). The Omo river project, reconnaissance geology and geochemistry of parts of Ilubabor, Kefa, Gemu Gofa and Sidamo, Ethiopia. *Ethiopian Institute of Geological Surveys*, *2*, 1–89.

Davidson, A., & Rex, D. C. (1980). Age of volcanism and rifting in southwestern Ethiopia. *Nature*, *283*(5748), 657–658. https://doi.org/10.1038/283657a0

Dindi, E. W. (1994). Crustal structure of the Anza graben from gravity and magnetic investigations. *Tectonophysics*, *236*(1–4), 359–371. https://doi.org/10.1016/0040-1951(94)90184-8

Dunkelman, T. J., Rosendahl, B. R., & Karson, J. A. (1989). Structure and stratigraphy of the Turkana rift from seismic reflection data. *Journal of African Earth Sciences*, *8*(2–4), 489–510. https://doi.org/10.1016/S0899-5362(89)80041-7

Ebinger, C. J. (2018). Crust and mantle structure and the expression of extension in the Turkana Depression of Kenya and Ethiopia [Dataset]. International Federation of Digital Seismograph Networks. https://doi.org/10.7914/SN/Y1_2018

Ebinger, C. J., Oliva, S. J., Pham, T. Q., Peterson, K., Chindandali, P., Illsley-Kemp, F., et al. (2019). Kinematics of active deformation in the Malawi rift and Rungwe volcanic province, Africa. *Geochemistry, Geophysics, Geosystems*, *20*(8), 3928–3951. https://doi.org/10.1029/2019GC008354

Ebinger, C. J., Yemane, T., Harding, D. J., Tesfaye, S., Kelley, S., & Rex, D. C. (2000). Rift deflection, migration, and propagation: Linkage of the Ethiopian and Eastern rifts, Africa. *Geological Society of America Bulletin*, *112*(2), 163–176. https://doi.org/10.1130/0016-7606(2000)112<163:RDMAPL>2.0.CO;2

Ekström, G., Nettles, M., & Dziewonski, A. M. (2012). The global CMT project 2004-2010: Centroid-moment tensors for 13,017 earthquakes. *Physics of the Earth and Planetary Interiors*, *200–201*, 1–9. https://doi.org/10.1016/j.pepi.2012.04.002

Emry, E. L., Shen, Y., Nyblade, A. A., Flinders, A., & Bao, X. (2019). Upper mantle Earth structure in Africa from full-wave ambient noise tomography. *Geochemistry, Geophysics, Geosystems*, *20*(1), 120–147. https://doi.org/10.1029/2018GC007804

Foster, A. N., & Jackson, J. A. (1998). Source parameters of large African earthquakes: Implications for crustal rheology and regional kinematics. *Geophysical Journal International*, *134*(2), 422–448. https://doi.org/10.1046/j.1365-246x.1998.00568.x

Franceschini, Z., Cioni, R., Scaillet, S., Corti, G., Sani, F., Isola, I., et al. (2020). Recent volcano-tectonic activity of the Ririba rift and the evolution of rifting in South Ethiopia. *Journal of Volcanology and Geothermal Research*, *403*, 106989. https://doi.org/10.1016/j.jvolgeores.2020.106989

French, S. W., & Romanowicz, B. (2015). Broad plumes rooted at the base of the Earth's mantle beneath major hotspots. *Nature*, *525*(7567), 95–99. https://doi.org/10.1038/nature14876

Fritz, H., Abdelsalam, M., Ali, K. A., Bingen, B., Collins, A. S., Fowler, A. R., et al. (2013). Orogen styles in the East African Orogen: A review of the Neoproterozoic to Cambrian tectonic evolution. *Journal of African Earth Sciences*, *86*, 65–106. https://doi.org/10.1016/j.jafrearsci.2013.06.004

Furman, T., Nelson, W. R., & Elkins-Tanton, L. T. (2016). Evolution of the East African rift: Drip magmatism, lithospheric thinning and mafic volcanism. *Geochimica et Cosmochimica Acta*, *185*, 418–434. https://doi.org/10.1016/j.gca.2016.03.024

Gasperini, P., Lolli, B., & Vannucci, G. (2013). Body wave magnitude mb is a good proxy of moment magnitude Mw for small earthquakes (mb<4.5–5.0). *Seismological Research Letters*, *84*(6), 932–937. https://doi.org/10.1785/0220130105

GEOFON Data Centre. (1993). *GEOFON seismic network*. GFZ Data Services. Other/Seismic Network. https://doi.org/10.14470/TR560404

George, R., Rogers, N., & Kelley, S. (1998). Earliest magmatism in Ethiopia: Evidence for two mantle plumes in one flood basalt province. *Geology*, *26*(10), 923–926. https://doi.org/10.1130/0091-7613(1998)026<0923:EMIEEF>2.3.CO;2

Ghosh, A., Holt, W. E., & Flesch, L. M. (2009). Contribution of gravitational potential energy differences to the global stress field. *Geophysical Journal International*, *179*(2), 787–812. https://doi.org/10.1111/j.1365-246X.2009.04326.x

Global Volcanism Program. (2013). *Volcanoes of the world* (Vol. 4.8.7). Smithsonian Institution. https://doi.org/10.5479/si.GVP.VOTW4-2013

Guth, A. L. (2016). *Volcanic volumes associated with the Kenya Rift: Recognition and correction of preservation biases* (Vol. 420, pp. 31–42). Geological Society of London, Special Publication. https://doi.org/10.1144/SP420.3

Heimann, S., Isken, M., Kühn, D., Sudhaus, H., Steinberg, A., Vasyura-Bathke, H., et al. (2018). *Grond—A probabilistic earthquake source inversion framework. V. 1.0*. GFZ Data Services. https://doi.org/10.5880/GFZ.2.1.2018.003

Herring, T., King, R., & McClusky, S. (2010). *Introduction to GAMIT/GLOBK release 10.4, mass*. Institute of Technology.

Kanamori, H. (1983). Magnitude scale and quantification of earthquakes. *Tectonophysics*, *93*(3–4), 185–199. https://doi.org/10.1016/0040-1951(83)90273-1

Katumwehe, A. B., Abdelsalam, M. G., Atekwana, E. A., & Laó-Dávila, D. A. (2016). Extent, kinematics and tectonic origin of the Precambrian Aswa shear zone in eastern Africa. *Gondwana Research*, *34*, 241–253. https://doi.org/10.1016/j.gr.2015.03.007

Keir, D., Ebinger, C. J., Stuart, G. W., Daly, E., & Ayele, A. (2006). Strain accommodation by magmatism and faulting as rifting proceeds to breakup: Seismicity of the northern Ethiopian rift. *Journal of Geophysical Research*, *111*(B5), B05314. https://doi.org/10.1029/2005JB003748

Kissling, E., Kradolfer, U., & Maurer, H. (1995). *Program VELEST user's guide-Short Introduction*. Institute of Geophysics.

Klein, F. W. (2000). User's guide to HYPOINVERSE-2000, a Fortran program to solve for earthquake locations and magnitudes. *U.S. Geological Survey*, *02–171*, 123. https://doi.org/10.3133/ofr02171

Knappe, E., Bendick, R., Ebinger, C. J., Birhanu, Y., Lewi, E., Floyd, M., et al. (2020). Accommodation of East African rifting across the Turkana Depression. *Journal of Geophysical Research: Solid Earth*, *125*(2), e2019JB018469. https://doi.org/10.1029/2019JB018469

Kogan, L., Fisseha, S., Bendick, R., Reilinger, R., McClusky, S., King, R., & Solomon, T. (2012). Lithospheric strength and strain localization in continental extension from observations of the East African Rift. *Journal of Geophysical Research*, *117*(B3), B03402. https://doi.org/10.1029/2011JB008516

Koptev, A., Burov, E., Gerya, T., Le Pourhiet, L., Leroy, S., Calais, E., & Jolivet, L. (2018). Plume-induced continental rifting and break-up in ultra-slow extension context: Insights from 3D numerical modeling. *Tectonophysics*, *746*, 121–137. https://doi.org/10.1016/j.tecto.2017.03.025

Koptev, A. I., & Ershov, A. V. (2010). The role of the gravitational potential of the lithosphere in the formation of a global stress field. *Izvestiya - Physics of the Solid Earth*, *46*(12), 1080–1094. https://doi.org/10.1134/S1069351310120050

Kostrov, V. V. (1974). Seismic moment and energy of earthquakes, and seismic flow of rock. *Izvestiya, Academy of Sciences, USSR.: Physics of the solid Earth*, *1*, 23–44.

Kounoudis, R., Bastow, I., Ebinger, C., Darbyshire, F., Musila, M., Ogden, C., et al. (2023). Seismic imaging of heterogeneous lithosphere beneath the unusually broad Turkana Depression, *East Africa* (No. EGU23-12655).

Kounoudis, R., Bastow, I. D., Ebinger, C. J., Ogden, C. S., Ayele, A., Bendick, R., et al. (2021). Body-wave tomographic imaging of the Turkana depression: Implications for rift development and plume-lithosphere interactions. *Geochemistry, Geophysics, Geosystems*, *22*(8), e2021GC009782. https://doi.org/10.1029/2021gc009782

Lavayssière, A., Drooff, C., Ebinger, C., Gallacher, R., Illsley-Kemp, F., Oliva, S. J., & Keir, D. (2019). Depth extent and kinematics of faulting in the southern Tanganyika rift, Africa. *Tectonics*, *38*(3), 842–862. https://doi.org/10.1029/2018TC005379

Lindenfeld, M., Rümpker, G., Link, K., Koehn, D., & Batte, A. (2012). Fluid-triggered earthquake swarms in the Rwenzori region, East African rift—Evidence for rift initiation. *Tectonophysics*, *566*, 95–104. https://doi.org/10.1016/j.tecto.2012.07.010

Martínez-Garzón, P., Kwiatek, G., Ickrath, M., & Bohnhoff, M. (2014). MSATSI: A MATLAB package for stress inversion combining solid classic methodology, a new simplified user-handling, and a visualization tool. *Seismological Research Letters*, *85*(4), 896–904. https://doi.org/10.1785/0220130189

Marzocchi, W., Spassiani, I., Stallone, A., & Taroni, M. (2020). How to be fooled searching for significant variations of the *b*-value. *Geophysical Journal International*, *220*(3), 1845–1856. https://doi.org/10.1093/gji/ggz541

Mechie, J., Keller, G. R., Prodehl, C., Gaciri, S., Braile, L. W., Mooney, W. D., & Sandmeier, K. J. (1994). Crustal structure beneath the Kenya Rift from axial profile data. *Tectonophysics*, *236*(1–4), 179–200. https://doi.org/10.1016/0040-1951(94)90176-7

Morley, C. K. (1994). Interaction of deep and shallow processes in the evolution of the Kenya rift. *Tectonophysics*, *236*(1–4), 81–91. https://doi.org/10.1016/0040-1951(94)90170-8

Morley, C. K. (2020). Early syn-rift igneous dike patterns, northern Kenya Rift (Turkana, Kenya): Implications for local and regional stresses, tectonics, and magma-structure interactions. *Geosphere*, *16*(3), 890–918. https://doi.org/10.1130/ges02107.1

Morley, C. K., Karanja, F. M., Wescott, W. A., Stone, D. M., Harper, R. M., Wigger, S. T., & Day, R. A. (1999). AAPG studies in geology# 44, Chapter 2: Geology and geophysics of the western Turkana basins, Kenya.

Morley, C. K., Wescott, W. A., Stone, D. M., Harper, R. M., Wigger, S. T., & Karanja, F. M. (1992). Tectonic evolution of the northern Kenyan Rift. *Journal of the Geological Society*, *149*(3), 333–348. https://doi.org/10.1144/gsjgs.149.3.0333

Muirhead, J. D., Fischer, T. P., Oliva, S. J., Laizer, A., van Wijk, J., Currie, C. A., et al. (2020). Displaced cratonic mantle concentrates deep carbon during continental rifting. *Nature*, *582*(7810), 67–72. https://doi.org/10.1038/s41586-020-2328-3

Muirhead, J. D., Scholz, C. A., & Rooney, T. (2022). Transition to magma-driven rifting in the South Turkana basin, Kenya: Part 1. *Journal of the Geological Society*, *179*(6), jgs2021–159. https://doi.org/10.1144/jgs2021-159

Muluneh, A. A., Brune, S., Illsley-Kemp, F., Corti, G., Keir, D., Glerum, A., et al. (2020). Mechanism for deep crustal seismicity: Insight from modeling of deformation processes at the Main Ethiopian Rift. *Geochemistry, Geophysics, Geosystems*, *21*(7), e2020GC008935. https://doi.org/10.1029/2020gc008935

Muluneh, A. A., Keir, D., & Corti, G. (2021). Thermo-rheological properties of the Ethiopian lithosphere and evidence for transient fluid induced lower crustal seismicity beneath the Ethiopian Rift. *Frontiers in Earth Science*, *260*. https://doi.org/10.3389/feart.2021.610165

Naliboff, J. B., Lithgow-Bertelloni, C., Ruff, L. J., & de Koker, N. (2012). The effects of lithospheric thickness and density structure on Earth′ s stress field. *Geophysical Journal International*, *188*(1), 1–17. https://doi.org/10.1111/j.1365-246X.2011.05248.x

Ogden, C. S., Bastow, I. D., Ebinger, C., Ayele, A., Kounoudis, R., Musila, M., et al. (2023). The development of multiple phases of superposed rifting in the Turkana Depression, East Africa: Evidence from receiver functions. *Earth and Planetary Science Letters*, *609*, 118088. https://doi.org/10.1016/j.epsl.2023.118088

Ogden, C. S., Keir, D., Bastow, I. D., Ayele, A., Marcou, S., Ugo, F., et al. (2021). Seismicity and crustal structure of the southern Main Ethiopian rift: New evidence from Lake Abaya. *Geochemistry, Geophysics, Geosystems*, *22*(8), e2021GC009831. https://doi.org/10.1029/2021GC009831

Oliva, S. J., Ebinger, C. J., Wauthier, C., Muirhead, J. D., Roecker, S. W., Rivalta, E., & Heimann, S. (2019). Insights into fault-magma interactions in an early-stage continental rift from source mechanisms and correlated volcano-tectonic earthquakes. *Geophysical Research Letters*, *46*(4), 2065–2074. https://doi.org/10.1029/2018GL080866

Philippon, M., Corti, G., Sani, F., Bonini, M., Balestrieri, M. L., Molin, P., et al. (2014). Evolution, distribution, and characteristics of rifting in southern Ethiopia. *Tectonics*, *33*(4), 485–508. https://doi.org/10.1002/2013TC003430

Pik, R., Marty, B., & Hilton, D. R. (2006). How many mantle plumes in Africa? The geochemical point of view. *Chemical Geology*, *226*(3–4), 100–114. https://doi.org/10.1016/j.chemgeo.2005.09.016

Prodehl, C., Jacob, A. W. B., Thybo, H., Dindi, E., & Stangl, R. (1994). Crustal structure on the northeastern flank of the Kenya rift. *Tectonophysics*, *236*(1–4), 271–290. https://doi.org/10.1016/0040-1951(94)90180-5

Purcell, P. G. (2018). Re-Imagining and re-imaging the development of the East African rift. *Petroleum Geoscience*, *24*(1), 21–40. https://doi.org/10.1144/petgeo2017-036

Reilinger, R., McClusky, S., Vernant, P., Lawrence, S., Ergintav, S., Cakmak, R., et al. (2006). GPS constraints on continental deformation in the Africa-Arabia-Eurasia continental collision zone and implications for the dynamics of Plate interactions. *Journal of Geophysical Research*, *111*(B5), B05411. https://doi.org/10.1029/2005JB004051

Ritsema, J., Deuss, A., van Heijst, H. J., & Woodhouse, J. H. (2011). S40RTS: A degree-40 shear-velocity model for the mantle from new Rayleigh wave dispersion, teleseismic travel time and normal-mode splitting function measurements. *Geophysical Journal International*, *184*(3), 1223–1236. https://doi.org/10.1111/j.1365-246X.2010.04884.x

Saria, E., Calais, E., Altamimi, Z., Willis, P., & Farah, H. (2013). A new velocity field for Africa from combined GPS and DORIS space geodetic solutions: Contribution to the definition of the African reference fame (AFREF). *Journal of Geophysical Research - Solid Earth*, *118*(4), 1677–1697. https://doi.org/10.1002/jgrb.50137

Schofield, N., Newton, R., Thackrey, S., Watson, D., Jolley, D., & Morley, C. (2021). Linking surface and subsurface volcanic stratigraphy in the Turkana depression of the East African rift system. *Journal of the Geological Society*, *178*(1). https://doi.org/10.1144/jgs2020-110

Scholz, C. H. (2015). On the stress dependence of the earthquake b value. *Geophysical Research Letters*, *42*(5), 1399–1402. https://doi.org/10.1002/2014GL062863

Shah, E. (1986). Seismicity of Kenya (Doctoral dissertation).

Snoke, J. A. (1984). A program for focal mechanism determination by combined use of polarity and SV-P amplitude ratio data. *Earthquake Notes*, *55*, 15.

Stamps, D. S., Flesch, L. M., & Calais, E. (2010). Lithospheric buoyancy forces in Africa from a thin sheet approach. *International Journal of Earth Sciences*, *99*(7), 1525–1533. https://doi.org/10.1007/s00531-010-0533-2

Stamps, D. S., Kreemer, C., Fernandes, R., Rajaonarison, T. A., & Rambolamanana, G. (2021). Redefining east African rift system kinematics. *Geology*, *49*(2), 150–155. https://doi.org/10.1130/G47985.1

Steiner, R. A., Rooney, T. O., Girard, G., Rogers, N., Ebinger, C. J., Peterson, L., & Phillips, R. K. (2022). Initial Cenozoic magmatic activity in East Africa: New geochemical constraints on magma distribution within the Eocene continental flood basalt province. *Geological Society, London, Special Publications*, *518*(1), 435–465. https://doi.org/10.1144/sp518-2020-262

Stern, R. J., Ali, K. A., Abdelsalam, M. G., Wilde, S. A., & Zhou, Q. (2012). U–Pb zircon geochronology of the eastern part of the Southern Ethiopian Shield. *Precambrian Research*, *206*, 159–167. https://doi.org/10.1016/j.precamres.2012.02.008

Sullivan, G. (2023). Kinematics of rift linkage between the eastern and Ethiopian rifts in the Turkana depression. MSc dissertation. Tulane University.

Teklay, M., Kröner, A., Mezger, K., & Oberhänsli, R. (1998). Geochemistry, Pb/Pb single zircon ages and Nd/Sr isotope composition of Precambrian rocks from southern and eastern Ethiopia: Implications for crustal evolution in East Africa. *Journal of African Earth Sciences*, *26*(2), 207–227. https://doi.org/10.1016/S0899-5362(98)00006-2

Torres Acosta, V., Bande, A., Sobel, E. R., Parra, M., Schildgen, T. F., Stuart, F., & Strecker, M. R. (2015). Cenozoic extension in the Kenya Rift from low-temperature thermochronology: Links to diachronous spatiotemporal evolution of rifting in East Africa. *Tectonics*, *34*(12), 2367–2386. https://doi.org/10.1002/2015TC003949

Vavryčuk, V. (2014). Iterative joint inversion for stress and fault orientations from focal mechanisms. *Geophysical Journal International*, *199*(1), 69–77. https://doi.org/10.1093/gji/ggu224

Waldhauser, F., & Ellsworth, W. L. (2000). A double-difference earthquake location algorithm: Method and application to the northern Hayward fault, California. *Bulletin of the Seismological Society of America*, *90*(6), 1353–1368. https://doi.org/10.1785/0120000006

Weinstein, A., Oliva, S. J., Ebinger, C. J., Roecker, S., Tiberi, C., Aman, M., et al. (2017). Fault-magma interactions during early continental rifting: Seismicity of the Magadi-Natron-Manyara basins, Africa. *Geochemistry, Geophysics, Geosystems*, *18*(10), 3662–3686. https://doi.org/10.1002/2017GC007027

Wescott, W. A., Wigger, S. T., Stone, D. M., & Morley, C. K. (1999). Geology and geophysics of the Lotikipi plain. In C. K. Morley (Ed.), *Geoscience of rift systems-evolution of East Africa*, *AAPG studies in geology* (Vol. 44, pp. 55–66). The American Association of Petroleum Geologists.

Westerhof, A. B., Härmä, P., Isabirye, E., Katto, E., Koistinen, T., Kuosmanen, E., & Virransalo, P. (2014). *Geology and geodynamic development of Uganda with explanation of the 1: 1,000,000 scale geological map*. Geological survey of Finland.

Woessner, J., & Wiemer, S. (2005). Assessing the quality of earthquake catalogues: Estimating the magnitude of completeness and its uncertainty. *Bulletin of the Seismological Society of America*, *95*(2), 684–698. https://doi.org/10.1785/0120040007

Zheng, W., Oliva, S. J., Ebinger, C., & Pritchard, M. E. (2020). Aseismic deformation during the 2014 M w 5.2 Karonga earthquake, Malawi, from satellite interferometry and earthquake source mechanisms. *Geophysical Research Letters*, *47*(22), e2020GL090930. https://doi.org/10.1029/2020GL090930

References From the Supporting Information

Anderson, J. A., & Wood, H. O. (1925). Description and theory of the torsion seismometer. *Bulletin of the Seismological Society of America*, *15*(1), 1–72.

Aki, K. (1965). *Maximum likelihood estimate of b in the formula log N= a-bM* and its confidence limits (Vol. 43, pp. 237–239). Bulletin of the Earthquake Research Institute-University of Tokyo.

Condori, C., Tavera, H., Marotta, G. S., Rocha, M. P., & França, G. S. (2017). Calibration of the local magnitude scale (ML) for Peru. *Journal of Seismology*, *21*(4), 987–999. https://doi.org/10.1007/s10950-017-9647-3

Dahm, T., Heimann, S., Funke, S., Wendt, S., Rappsilber, I., Bindi, D., et al. (2018). Seismicity in the Block Mountains between Halle and Leipzig, Central Germany: Centroid moment tensors, ground motion simulation, and felt intensities of two $M \approx 3$ earthquakes in 2015 and 2017. *Journal of Seismology*, *22*(4), 985–1003. https://doi.org/10.1007/s10950-018-9746-9

Dziewonski, A. M., Chou, T.-A., & Woodhouse, J. H. (1981). Determination of earthquake source parameters from waveform data for studies of global and regional seismicity. *Journal of Geophysical Research*, *86*(B4), 2825–2852. https://doi.org/10.1029/JB086iB04p02825

Ebinger, C. J., & Ibrahim, A. (1994). Multiple episodes of rifting in central and East Africa: A re-evaluation of gravity data. *Geologische Rundschau*, *83*(4), 689–702. https://doi.org/10.1007/bf00251068

Ebinger, C. J., Yemane, T., Woldegabriel, G., Aronson, J. L., & Walter, R. C. (1993). Late Eocene–Recent volcanism and faulting in the southern main Ethiopian rift. *Journal of the Geological Society*, *150*(1), 99–108. https://doi.org/10.1144/gsjgs.150.1.0099

Gutenberg, B., & Richter, C. F. (1954). *Seismicity of the Earth and related phenomena*. Princeton University Press.

Heimann, S., Kriegerowski, M., Isken, M., Cesca, S., Daout, S., Grigoli, F., et al. (2017). Pyrocko—An open-source seismology toolbox and library. https://doi.org/10.5880/GFZ.2.1.2017.001

Hutton, L. K., & Boore, D. M. (1987). The ML scale in southern California. *Bulletin of the Seismological Society of America*, *77*(6), 2074–2094. https://doi.org/10.1785/bssa0770062074

Illsley-Kemp, F., Keir, D., Bull, J. M., Ayele, A., Hammond, J. O., Kendall, J. M., et al. (2017). Local earthquake magnitude scale and b-value for the Danakil region of northern Afar. *Bulletin of the Seismological Society of America*, *107*(2), 521–531. https://doi.org/10.1785/0120150253

Richter, C. F. (1935). An instrumental earthquake magnitude scale. *Bulletin of the Seismological Society of America*, *25*(1), 1–32. https://doi.org/10.1785/BSSA0250010001

Wang, R. (1999). A simple orthonormalization method for stable and efficient computation of Green's functions. *Bulletin of the Seismological Society of America*, *89*(3), 733–741. https://doi.org/10.1785/BSSA0890030733

Winn, R. D., Steinmetz, J. C., & Kerekgyarto, W. L. (1993). Stratigraphy and rifting history of the Mesozoic-Cenozoic Anza rift, Kenya. *AAPG Bulletin*, *77*(11), 1989–2005. https://doi.org/10.1306/bdff8f9c-1718-11d7-8645000102c1865d